PORTLAND PRESS

BIOCHEMICAL JOURNAL
ACCEPTED MANUSCRIPT

Modulation of prion polymerization and toxicity by rationally designed peptidomimetics

Ankit Srivastava, Sakshi Sharma, Sandhya Sadanandan, Sakshi Gupta, Jasdeep Singh, Sarika Gupta, V. Haridas, Bishwajit Kundu

Misfolding and aggregation of cellular prion protein (PrPC) is associated with a large array of neurological disorders commonly called the Transmissible spongiform encephalopathies (TSEs). Designing inhibitors against prions has remained a daunting task owing to limited information about mechanism(s) of their pathogenic self-assembly. Here, we explore the anti-prion properties of a combinatorial library of bispidine-based peptidomimetics (BPMs) that conjugate amino acids with hydrophobic and aromatic side chains. Keeping the bispidine unit unaltered, a series of structurally diverse BPMs were synthesized and tested for their prion modulating properties. Administration of Leu- and Trp-BPMs delayed and completely inhibited the amyloidogenic conversion of human prion protein (HuPrP), respectively. We found that each BPM induced the HuPrP to form unique oligomeric nanostructures differing in their biophysical properties, cellular toxicities and response to conformation-specific antibodies. While Leu-BPMs were found to stabilize the oligomers, Trp-BPMs effected transient oligomerization resulting in the formation of non-toxic, non-fibrillar aggregates. Yet another aromatic residue Phe however, accelerated the aggregation process in HuPrP. Molecular insights obtained through MD simulations suggested that each BPM differently engage a conserved Tyr 169 residue at the α2-β2 loop of HuPrP and affect the stability of α2 & α3 helices. Our results demonstrate that this new class of molecules having chemical scaffolds conjugating hydrophobic/aromatic residues could effectively modulate prion aggregation and toxicity.

Cite as Biochemical Journal (2016) DOI: 10.1042/BCJ20160737

Modulation of prion polymerization and toxicity by rationally designed peptidomimetics

Ankit Srivastava[1], Sakshi Sharma[2], Sandhya Sadanandan[2], Sakshi Gupta[3], Jasdeep Singh[1], Sarika Gupta[3], V. Haridas[2]*, Bishwajit Kundu[2]*

[1]Kusuma School of Biological Sciences, [2]Department of Chemistry; IIT Delhi, New Delhi, India, [3]Molecular Sciences Laboratory, National Institute of Immunology, New Delhi, India.

*To whom correspondences should be addressed: Dr. B. Kundu, email: bkundu@bioschool.iitd.ac.in, Dr. V. Haridas, email: haridasv@chemistry.iitd.ac.in.

Misfolding and aggregation of cellular prion protein (PrP^C) is associated with a large array of neurological disorders commonly called the Transmissible spongiform encephalopathies (TSEs). Designing inhibitors against prions has remained a daunting task owing to limited information about mechanism(s) of their pathogenic self-assembly. Here, we explore the anti-prion properties of a combinatorial library of bispidine-based peptidomimetics (BPMs) that conjugate amino acids with hydrophobic and aromatic side chains. Keeping the bispidine unit unaltered, a series of structurally diverse BPMs were synthesized and tested for their prion modulating properties. Administration of Leu- and Trp-BPMs delayed and completely inhibited the amyloidogenic conversion of human prion protein (HuPrP), respectively. We found that each BPM induced the HuPrP to form unique oligomeric nanostructures differing in their biophysical properties, cellular toxicities and response to conformation-specific antibodies. While Leu-BPMs were found to stabilize the oligomers, Trp-BPMs effected transient oligomerization resulting in the formation of non-toxic, non-fibrillar aggregates. Yet another aromatic residue Phe however, accelerated the aggregation process in HuPrP. Molecular insights obtained through MD simulations suggested that each BPM differently engage a conserved Tyr 169 residue at the α2-β2 loop of HuPrP and affect the stability of α2 & α3 helices. Our results demonstrate that this new class of molecules having chemical scaffolds conjugating hydrophobic/aromatic residues could effectively modulate prion aggregation and toxicity.

Key words: Prion, Amyloid, Bispidine, Oligomer, toxicity, protein misfolding

Summary statement: Few hydrophobic/aromatic amino acids alone or in combination, when conjugated with bispidine scaffold were found to influence prion fibrillization and toxicity. Comprehensive mechanistic insight of the process is demonstrated and is projected as a new strategy for amyloid inhibition.

Short Title: Bispidine peptidomimetics influence prion amyloidogenesis.

INTRODUCTION

Self-assembly of biological macromolecules into ordered structures regulates several biological processes and is a critical determinant of normal or diseased states (1). Amyloid aggregation is a self-assembly process that has been found associated with several systemic and neurodegenerative diseases and disorders (2). Transmissible spongiform encephalopathies (TSEs) are a class of fatal neurodegenerative diseases that arise due to the conversion of cellular prion protein (PrP^{C}) into an aberrant pathogenic conformation, the 'scrapie' form (PrP^{Sc}) (3, 4). Several forms of TSEs in humans and animals are identified that include kuru disease, Creutzfeldt-Jakob disease, fatal familial insomnia, Gerstmann-Straussler-Scheinker syndrome, scrapie and bovine spongiform encephalopathy (5, 6). This abnormal form is characterized as infectious aggregates that deposit as plaques. The process follows a nucleation-dependent polymerization mechanism, generating oligomeric intermediates, before resting as β-sheet rich amyloid fibrils (7, 8). Polymerization begins as a critical nucleus on which monomeric or oligomeric prion molecules associate (9). Following this a series of intermediates of different sizes and molecular organizations emerge, some of which then enter into a burst phase of rapid association to attain the final fibrillar form. The nucleation phase as well as the early- and mid-phase intermediates get kinetically partitioned to either productive fibril by continuous association (*on-pathway*), or terminate into discrete, non-fibrillar, oligomeric species (*off-pathway*) (10-12). Consequently, successful amyloidogenic inhibitors are those which can either trap and stabilize the early oligomers, or guide the polymerization event in favor of non-productive, *off-pathway* intermediates (13-17). Besides several other inhibition strategies such as kinetic or thermodynamic stabilization of the monomeric precursors, β-sheet breaker peptides, chaperone mediated intervention, fibril disaggregating molecules, have been reported recently (18-23). While all the above mentioned strategies have been tested, only limited therapeutic success has been achieved (24-26). This is primarily attributed to poor understanding of the molecular mechanism(s) of amyloid conversion and limited information about the amino acids involved in the assembly process.

Evidences from inter-species transmission of prion strains suggests that certain species such as rabbit, horse and all marsupials show surprising resistance to prion diseases (27-29). The structural features of most vertebrate prion proteins consists of a largely α-helical fold with small amount of β-sheet and random coils (30). Evidently, this α-helical form (PrP^{C}) converts into a predominantly β-sheet-rich 'scrapie' form (PrP^{Sc}) that matures into amyloids with a protease resistant core (31, 32). This protease resistant fragment comprises prion residues 90-231 displays attributes of PrP^{Sc}, is infectious and has been shown to accumulate in scrapie infected brains (33-36). Thus, it is considered the 'core' of the infectious agent and has been widely utilized for investigating self assembly, aggregation and infectivity in prions(37-39). It has been shown to misfold and aggregate under mild denaturing conditions into amyloid fibrils exhibiting 'scrapie' (PrP^{sc}) like characteristics (40, 41). The NMR structure of recombinant human PrP 90-231 (HuPrP) encompasses a disordered N-terminal region (90-121) along with a structured, globular C-terminal domain (122-231) consisting of three α-helices (α1, α2 and α3), two short anti-parallel β-strands (β1 and β2) and two connecting loops (α2-α3 loop and β2-α2 loop) (Figure 1A). Previous reports have indicated that these secondary structural components play important role in conversion of PrP^{C} into PrP^{Sc}. Misfolding events in PrP^{C} may get initiated by conversion of the α1 into a left-handed β-helix conformation (42, 43). In addition, the unfolding and β-sheet conversion of α2-α3 region during the course of prion aggregation has also been shown (44, 45). These experimental evidences are largely supported by computational studies highlighting the intrinsic instability and β-sheet propensities of these helices. Consequently, the amino acids in these discordant helices although responsible for structural rigidity, under pathogenic conditions may as well drive conformational conversion to scrapie form. This conversion largely depends on interaction between the hydrophobic and aromatic residues in these helices (46-48). Several reports indicate that such interactions indeed form the driving force in acquisition of protease resistant core by prions and modulate their neurotoxicity (49-51).

In the present study, we explore a new strategy by conjugating few aromatic and hydrophobic amino acids with a non-biological scaffold to create discrete peptidomimetics. Peptidomimetics owing to their non-canonical and semi-rigid backbones can exist in specific conformations and thus have been utilized for multitude of functions. Previously, different peptidomimetic scaffolds have been tested on diverse protein targets and as potential antimicrobial agents (52, 53). Besides, their considerable thermodynamic stability and resistance to various proteases also makes them good therapeutic candidates (54, 55). In our case, introduction of hydrophobic/aromatic amino acid on an appropriate scaffold is envisioned by us as a strategy to influence the aggregation of prion protein. This method clearly deviates from the one in which additional aromatic and hydrophobic amino acids are incorporated and made a part of the polypeptide chain. The molecular architecture of conjugated hydrophobic/aromatic residues could modulate and control the complex process of $PrP^{C} \rightarrow PrP^{Sc}$ conversion. We hypothesized that the bicyclic rigid bispidine unit (3,7-diazabicyclo [3.3.1] nonane) with two nitrogen atoms at ~2.8 Å is ideal to append amino acids for interfering with protein-protein interactions (56). Bispidine is a versatile secondary structure nucleator (57). Its hydrophobicity and rigidity could enable interaction with hydrophobic surfaces and can orient the conjugated amino acids in defined geometrical arrangements for additional interactions. Further, the amino acid side chains could interfere with the non-covalent interactions during the misfolding of different helices (α1, α2 and α3) and may thus influence prion aggregation. Based on this hypothesis, we synthesized a combinatorial library of Bispidine-based peptidomimetics (BPMs) that appended different combinations of hydrophobic/aromatic residues (Phe, Leu and Trp) and tested their effect on the amyloidogenesis of human prion protein (HuPrP) (Figure1B). All the BPMs were synthesized by typical peptide coupling reaction between bispidine scaffold and N-protected amino acids (Figure 2). The protected bispidine derivative was functionalized with appropriate N-protected amino acids to obtain a variety of BPMs (See Supplementary methods; Supplementary Figures S1-S27). The BPMs thus synthesized were named as; Phe (**B1**, **B2**); Leu (**B3**, **B4**, **B5**); Leu and Phe (**B6**); Trp (**B7**, **B8**, **B9**, **B10**) and Lys (**B11**).

MATERIALS AND METHODS

Chemical Reagents

All reagents used in the present study were of the highest purity grade from Sigma-Aldrich, unless otherwise specified. All amino acids used were of L-configuration unless otherwise stated. All solvents were dried using appropriate drying agent prior to use. Reactions were monitored by thin layer chromatography (TLC). Silica gel G (Merck) was used for TLC and column chromatography was done on silica gel (100-200 mesh) columns, which were generally made from slurry in hexane, hexane/ethyl acetate or chloroform. Melting points were recorded in a Fisher-Johns melting point apparatus and were uncorrected. Optical rotations were measured with a Rudolph Research Analytical Autopol® V Polarimeter; concentrations are given in grams/mL. IR spectra were recorded on a Nicolet, Protégé 460 spectrometer as KBr pellets. ^{1}H NMR spectra were recorded on Bruker-DPX-300 (^{1}H, 300 MHz; ^{13}C, 75 MHz) spectrometer using tetramethylsilane (^{1}H) as an internal standard. Coupling constants are in Hz and the ^{1}H NMR data are reported as s (singlet), d (doublet), br (broad), br d (broad doublet), t (triplet), q (quartet) and m (multiplet). HRMS were recorded with AB Sciex, 1011273/A model using ESI-technique.

Compound synthesis and purification

All BPMs were synthesized following our previously described protocol with some modifications (57). To an ice-cold solution of Boc/Z-protected amino acid (1.65 mmol) in 65 mL of dry dichloromethane, N-hydroxysuccinimide (1.65 mmol), N,N'-dicyclohexylcarbodiimide (1.65 mmol) were added and stirred for 10 min. Following this, bispidine (0.75 mmol) and triethylamine (0.192 mL, 1.65 mmol) were added. The reaction mixture was stirred overnight, filtered and washed with 0.2 N H_2SO_4, saturated aqueous $NaHCO_3$ and finally with water. The organic layer was dried over anhydrous Na_2SO_4, filtered and evaporated to yield the crude product. It was then purified by silica gel chromatography.

For the selective removal of N-Boc Group, **B9** (1 mmol) was dissolved in 500 mol % of a 1 M solution of HCl in ethyl acetate (prepared by bubbling dry HCl into dry ethyl acetate then diluting to 1 M with additional ethyl acetate). The reaction mixture was stirred at room temperature until the disappearance of starting material as determined by TLC (typically 3-5 h). The precipitated product (**B10**) was isolated by filtration. The information on chemical characterization of BPMs is given as supplementary data (Supplementary Figures S1-S27).

Preparation of recombinant human prion protein (HuPrP)

The human prion (HuPrP) comprising the residues of structural unit (90-231) was expressed as recombinant, His-tagged protein and purified as described previously with minor modifications (58). Briefly, the bacterially expressed inclusion bodies were solubilized after sonication in lysis buffer (100 mM Na_2PO_4, 8M urea, 10 mM reduced glutathione, pH 8.0) and loaded on a pre-equilibrated Ni-NTA column in batch mode. The protein was eluted in 500 mM imidazole (pH 5.8) following an on-column refolding procedure using a decreasing gradient of urea in lysis buffer. The eluted protein was extensively dialyzed firstly against 100 mM Na_2PO_4 (pH 5.8) followed by milliQ water and lyophilized until further use. The concentration of the purified protein was determined by measurement of absorbance at 280 nm (A_{280}), using the extinction coefficient ε_{280} = 22015 $M^{-1}cm^{-1}$.

Preparation of recombinant α-Synuclein and $IAPP_{20-29}$

Recombinant α-synuclein was expressed and purified as described elsewhere (59). Briefly, the bacterial cell pellets containing expressed protein were resuspended in Tris buffer (50 mM, pH 7.5) containing 10 mM EDTA and 150 mM NaCl and were stored at -80 °C. The frozen cells were lysed by incubating in boiling water bath for 5-10 min and the supernatant was collected by centrifugation. Following this, ammonium sulphate precipitation was carried out and the pellet was washed and resuspended in 100 mM ammonium acetate. Next, the precipitation reaction was carried out twice using equal volume of ethanol at room temperature. Finally, the obtained pellet was resuspended in ammonium acetate and dialyzed extensively against Tris-HCl buffer (10 mM, pH 7.4). The protein was confirmed using SDS-PAGE and was stored at -80 °C until further use. The synthetic $IAPP_{20-29}$ decapeptide (20-SNNFGAILSS-$CONH_2$-29) was procured (Biocell Inc., India) with a purity of >95% and confirmed by mass spectrometry and HPLC.

Fluorescent labeling

Purified HuPrP was dialyzed overnight at 4 ^oC against 50 mM phosphate buffer (pH 7.0). Following dialysis, protein was labeled using fluorescein isothiocyanate (FITC, Sigma) dissolved in anhydrous DMSO at 1 mg/ml. A 20:1 labeling ratio (F:P) was used and the mixture was left for conjugation in dark for 4h at 4 ^oC. The resulting FITC-HuPrP solution ($HuPrP^{FITC}$) was dialyzed against 50 mM phosphate buffer (pH 7.0) four times for 6 hours each in dark at 4 ^oC to remove any unconjugated FITC. After determining the concentration of $HuPrP^{FITC}$ using extinction coefficient (ε_{280}=22015 $M^{-1}cm^{-1}$), the F: P ratio was calculated as per manufacturer's protocol using a ratio of FITC absorption at 280 versus 495 nm of 0.35.

Amyloid aggregation experiments

The α-monomeric form of the HuPrP was taken at a concentration of 30 µM in phosphate buffer (50mM, pH 7.0) containing 0.5 M guanidine hydrochloride and 0.02 % (v/v) final concentration of sodium azide (60). The samples were incubated in 1.5 ml eppendorfs at 37°C under continuous agitation at 200 rpm. The fibrillation of prion protein in the absence and presence of increasing molar concentration of compounds (1:1, 1:2 and 1:3 molar ratios) was monitored by fluorescence assay and Dynamic light scattering. For α-synuclein, aggregation was performed as described previously with minor modifications(61). Briefly, LMW α-Synuclein at a concentration of 100 µM in 20 mM Tris-HCL, 50 mM NaCl, pH 7.5 and 0.02 % (v/v) sodium azide (with or without compounds) was incubated in 1.5 ml eppendorfs.

The tubes were agitated at a speed of 500 r.p.m using a MX-M Microplate Mixer (SCILOGEX, LLC. USA) placed inside a 37 ^{o}C incubator. Similarly, $IAPP_{20-29}$ aggregation was performed as described previously with minor modifications (62). $IAPP_{20-29}$ peptide at a 100 µM concentration in 50 mM HEPES, pH 7.2 and 0.02 % (v/v) sodium azide (with or without compounds) was incubated in 1.5 ml eppendorfs. The tubes were agitated with a speed of 200 rpm at 37 ^{o}C as described above. The amyloid aggregation in both cases was monitored using ThT fluorescence assay and AFM imaging.

Thioflavin T fluorescence assay

The amyloid formation kinetics was monitored using the standard Thioflavin T (ThT) fluorescence assay. At increasing time points, aliquots (10 µl) were drawn from each sample and mixed with 10 µM of ThT in 50 mM phosphate buffer (pH 7), and incubated for 10 min. Fluorescence measurements were done in a 1 cm path length cuvette using a LS 55 fluorescence spectrometer (PerkinElmer, MA, USA). The excitation and emission wavelengths were kept at 450 and 485 nm, respectively. The excitation and emission slit width were kept at 5 nm and 10 nm respectively. All data from triplicate reactions for each compound concentration was averaged and fitted using the following sigmoid equation in origin 8.0. (Equation 1) as described earlier (63).

$$\boldsymbol{Y = (Y_i + m_i x) + \frac{V_f + m_f x}{\left[1 + \exp\frac{-(x - x_{50})}{\tau}\right]}} \qquad \textbf{(1)}$$

Here, Y is ThT fluorescence intensity (a.u.), x is time in hours and x_{50} is the time at which ThT fluorescence reached 50% of the maximum intensity ($Intensity_{max}$). The nucleation or the lag time of aggregation is given by (equation 2).

$$\boldsymbol{T_{lag} = x_{50} - 2\tau} \qquad \textbf{(2)}$$

Fluorescence binding assay

For binding assay, steady state fluorescence studies using a LS 55 fluorescence spectrophotometer (PerkinElmer, MA, USA) were performed. Since, the BPMs incorporate aromatic residues (Phe- in **B1** and **B6**; Trp- in **B9**), we utilized FITC labelled protein ($HuPrP^{FITC}$). The fluorescence assay was based on the assumption that binding of BPMs to $HuPrP^{FITC}$ affects the quantum yield of fluorophore as compared to free $HuPrP^{FITC}$ and therefore a change in fluorescence should take place. Protein solution of 5 µM was titrated using continuous injections from individual BPM stock solutions of 100 µM (10 µM in case of **B9**) concentration. The excitation wavelength (λ_{ex}) was fixed at 495 nm, emission scans were recorded between 500 and 600 nm (λ_{em} =525 nm), keeping the excitation and emission slits set at 5 nm and 2.5 nm respectively. All fluorescence measurements were performed in 50 mM phosphate buffer (pH 7.0) in triplicates with 3 accumulations each after a pre-scan incubation of 5 minutes and averaged. The bound fraction versus total ligand concentration was analysed using one-site binding model of association as given below:

$$\mathbf{P + L \leftrightarrows PL}$$

$$\boldsymbol{K_p = \frac{[PL]}{[P][L]}}$$

Here, P and L represent the protein ($HuPrP^{FITC}$) and compound (BPMs) concentrations respectively and K_p is the association constant. A double reciprocal plot of change in fluorescence intensity (1/dF) at 525 nm (λ_{ex}=495 nm) for each point of titration versus ligand concentration (1/BPM concentration) was used to determine dF_{max}. The dF_{max} parameter is defined as change in fluorescence intensity from the initial fluorescence or the fluorescence of free protein (F_o). Finally, the fraction bound (dF/dF_{max}) versus total ligand (BPM) concentration was best fitted to one-site binding model given by equation 3.

$$\mathbf{Y = \frac{B_{max} X}{(K_d + X)}} \qquad \textbf{(3)}$$

Where, X is concentration of ligand (µM), Y is specific binding, B_{max} is maximum binding and K_d is the apparent dissociation constant. The free energy of binding was derived using equation 4.

$$\mathbf{\Delta G_{binding} = -RT \ln K_d} \qquad \textbf{(4)}$$

Here, $\Delta G_{binding}$ represents binding free energy change, T is temperature and R is the universal gas constant (1.98 cal K^{-1} mol^{-1}).

Transmission Electron Microscopy (TEM)

The transmission electron micrographs of aggregating samples were acquired using the Tecnai trans-mission electron microscope (FEI, USA) operating at 120 kV. The HuPrP aggregates formed alone or in presence of BPMs **B1**, **B5**, **B6** and **B9** (1:3 molar ratio) obtained after 60 h incubation were 5-fold diluted and placed on a copper grid for 2 minutes. Following this, the samples were negatively stained using a 2% (w/v) uranyl acetate solution, washed with milliQ water, air dried and imaged.

Atomic Force Microscopy (AFM)

The AFM imaging of aggregating samples was done using a Bioscope Catalyst AFM (Bruker Corporation, Billerica, MA). The end-stage morphology of HuPrP aggregates formed alone or in presence of BPMs **B1**, **B5**, **B6** and **B9** (1:3 molar ratio) obtained after 60 h incubation was examined. Also, the oligomeric intermediates formed in presence of **B1** (12 h), **B5** (38 h), **B6** (12 h) and **B9** (24 h) at 1:3 molar ratio were examined. Aliquots of each sample were diluted 3 folds in 50 mM phosphate buffer, pH 7.0 and deposited on freshly cleaved mica. Following 10-15 min incubation, the samples were washed using milliQ water and dried under nitrogen. Samples were analyzed using standard tapping mode and resulting images were processed using Nanoscope analysis v.1.4.

Dynamic Light Scattering

Dynamic light scattering (DLS) measurements were utilized to ascertain the particle size variation of HuPrP aggregates formed alone or in presence of BPMs **B1**, **B5**, **B6** and **B9** (1:3 molar ratio). The data was acquired at 25 °C using a Malvern Zetasizer Nano ZS (Malvern Instruments, UK) containing a 3 mW Helium-Neon laser with a wavelength of 633 nm and a scattering angle of 173 degrees. For each sample the correlation time was defined at 10 seconds per run with 20 runs for each measurement. The aggregating samples in presence or absence of compounds at different time points were taken for the measurements. All samples were centrifuged and passed through 0.1 µm filters before transferring them to the cuvette for measurement. The dispersant viscosity and refractive index was kept at 0.89 mPa and of 1.34 respectively. The results were processed using Zetasizer software 6.01 and were represented as intensity of distribution (%) of particles versus hydrodynamic radius (nm).

ATR-FTIR

The attenuated total reflectance (ATR) FTIR spectroscopy was utilized to ascertain the secondary structural changes associated with HuPrP aggregates formed alone or in presence of BPMs **B1**, **B5**, **B6** and **B9** (1:3 molar ratio). All data was acquired on a Nicolet 800 FTIR spectrometer (Thermo Scientific, USA) with a MCT detector and purged with dry air. All aggregating solutions after 60 h incubation were concentrated ~ 10-12 folds using 10 kDa Amicon centrifugal filters (Millipore, USA). A drop of this solution was applied on the germanium crystal of the horizontal ATR sampling accessory and scanned. The data was acquired at a resolution of 4 cm^{-1} and 256 scans were averaged per sample after subtracting the buffer background. The second derivative of amide I region (1,700 cm^{-1} to 1,600 cm^{-1}) was fitted with least-squares iterative curve fitting to Gaussian line shapes in the raw spectra. The secondary structural assessment based on peak assignments was done as reported previously (64, 65).

Antibody Dot blot assay

The oligomeric intermediates formed in presence of **B1** (12 h), **B5** (38 h), **B6** (12 h) and **B9** (24 h) at 1:3 molar ratio were tested for their reactivity to A11 antibody (Millipore, USA). For dot blots, 8 µl of each oligomer sample (~ 4 µg total proteins) was spotted on nitrocellulose membrane and dried for one hour at 37°C. The membrane was blocked using TBST-5% (w/v) Tween 20, BSA and incubated with A11 antibody (1:1000 dilutions). Similarly, loading controls in each case was tested using anti-HuPrP antibody (D3Q5C, Cell Signaling Technology, Inc. USA) and anti-α-Synuclein antibody (D37A6, Cell Signaling Technology, Inc. USA). After washing for three times with TBS–0.1% Tween 20, the membrane was incubated for 2 h at room temperature with horseradish peroxidase-conjugated anti-rabbit IgG

(1:13000 dilution) (Santa Cruz Biotechnology). The membrane was subsequently washed with TBS–0.1% Tween 20 for three times. Specific protein bands were visualized with ECL chemiluminescence system (Bio-Rad Laboratories, Inc., Hercules, CA, USA).

MTT metabolic assay

About 2 x 10^4 SH-SY5Y cells were seeded in each well of a 96-well plate 24 h prior to treatment. The oligomer samples of HuPrP alone (24 h) and those formed in presence of **B1** (12 h), **B5** (38 h), **B6** (12 h), **B9** (24 h) were dialyzed at 4 ^{o}C against 50 mM phosphate buffer, pH 7.0 with 4 changes of 3 h each. Initially, increasing volumes of HuPrP oligomers were pre-tested to standardize their toxicity against SH-SY5Y cells. Addition of 20 µl (0.5 µM total protein) of HuPrP oligomers displayed ~50 % decrease in cell toxicity. An equivalent amount of oligomers formed in presence of **B1**, **B5**, **B6** and **B9** were added to SH-SY5Y cells in order to ascertain their toxicities. Dimethylthiazolyl-2-5-diphenyltetrazolium bromide (MTT) dye solution (Sigma, St. Louis, MO, USA) was added into the 96-well plate 24 h post treatment. The plate was incubated at 37°C for 4 h, and the treatment was terminated by adding elution buffer (isopropanol with 0.04 N HCl). MTT was cleared by live cells to a colored formazan product. Absorbance at 560 nm wavelength was recorded using a Bio-Rad micro plate reader 680 (Bio-Rad Laboratories, Inc., Hercules, CA, USA). Each treatment was repeated in triplicates. An averaged absorbance of blank values (containing all reagents except cells) was subtracted from all absorbance to yield corrected absorbance. The percentage cell viability was calculated with respect to untreated control cells.

Docking and complex selection

The structure of the human prion protein, HuPrP 90-231 (aqueous solution NMR structure, PDB 2KUN) was obtained from the Protein Data Bank (66). The chemical structures of BPMs (**B1**, **B5**, **B6** and **B9**) were drawn in a standard manner using ChemSketch. The energy minimization of generated structures was carried out using PRODRG employing GROMOS 96.1 force field (67). Further, the binding modes of compounds were identified using the BSP-SLIM (Binding Site Prediction and Shape based Ligand Matching) algorithm (68). Briefly, the holo-structures sharing similar global topology with the HuPrP structure were first identified and geometric centres of bound ligands in the holo-structures were clustered for identifying putative binding sites. A box centring the predicted binding sites was defined with successive grid filtering to extract the inner shape (negative image) of binding pockets. Following this, a shape and chemical feature comparison of multiple target ligand conformers with all negative images was done using the OMEGA program. Best overlays of each ligand conformer with the negative images were carried out using OEChem toolkit v.1.7 and the chemical features of ligands were assigned using Implicit-MillsDean color force field (69). Finally, all ligand conformations were sorted by docking scores and then categorized by RMSD tolerance value of 4 Å. For incorporating ligand flexibility in identifying optimal binding poses, the best docked complexes from BSP-SLIM were re-assessed by performing flexible docking using Molecular Operating Environment (MOE) v2009.105. The triangular matching placement method with London dG scoring function was employed to generate most favourable poses of ligand conformations by aligning ligand triplets of atoms with triplets of receptor site points. Finally, the molecular interactions of compounds were analyzed using Molegro molecular viewer v.2.2.

Molecular Dynamics Simulations

All atom explicit solvent MD simulations were carried out in GROMACS package v4.5.5. using CHARMM 27 force field (70). The Ligand topologies were generated using SwissParam (71).

All reduced structures were constrained using LINCS algorithm after adding hydrogen atoms. The solution NMR structure of human prion protein (PDB id: 2KUN) alone and its docked complexes with **B1**, **B5**, **B6** and **B9** were placed in cubical boxes, equidistantly at 12Å from box edges. The periodic boundary conditions were applied in all three dimensions following which the systems were explicitly solvated using TIP3P water system (72). Appropriate numbers of counter ions were added to neutralize the systems and to mimic physiological conditions. All systems were energy minimized by steepest

descent (2000 steps) and conjugant gradient (1000 steps) methods. In separate steps of 400 ps each, the systems were first equilibrated in an NVT ensemble followed by NPT ensemble. Particle mesh Ewald (PME) method was employed to treat long-range electrostatic interactions with a cut off radius of 10Å (73). Berendsen coupling was employed to maintain a constant system temperature of 300 K (74). The Leap frog integration was used to generate velocity coordinates of each system with 2 fs time step. Each system was simulated for 25 ns and structural coordinates were saved every 4 ps. The variation in backbone RMSD, Cα root mean square fluctuation (RMSF) and radius of gyration (Rg) of each protein ensemble was analyzed from the resulting trajectories. Further, the variation in distances between crucial residues (Asp 178-Tyr 128, Asp 178-Tyr 169, Gln 172-Tyr 218 and Tyr 169-Tyr 175) and individual Rg variations in the α2-α3 (Asn 173-Ser 231) helices during the simulation were analyzed using Gromacs tools. The structural coordinates were analyzed using PyMOL and Discovery Studio visualizer v.3.1.2.

RESULTS

Phe-BPMs accelerate prion polymerization

The effect of BPMs on amyloidogenesis was investigated by monitoring the aggregation of HuPrP (30 μM) in the presence of increasing molar ratios of BPMs. ThT fluorescence exhibited by aggregating samples is attributed to the presence of fibrillar content (75). Time lapse ThT fluorescence measurements have been widely utilized for monitoring amyloid forming kinetics of variety of proteins (7, 63, 64, 76). The flat portion of the curve at the beginning of amyloid kinetics is termed as lag-time (t_{lag}). The lag-time represents the nucleation period and its end represents monomer depletion due to association in the form of aggregates (77). Thus, any influence on aggregating monomers may essentially alter the lag-time during the amyloid formation. The ThT fluorescence of HuPrP amyloidogenic reaction, in the absence of any BPMs, followed a typical sigmoidal trend with a distinct lag phase of ~24 h, an exponential phase up to 45 h, reaching stationary phase at the end of 60 h (black traces, Figure 3, Table 1). The presence of a distinct lag phase corroborated with previously reported nucleation-dependent polymerization phenomenon in human prion protein (78). Formation of fibrillar aggregates at the stationary phase was confirmed by TEM imaging (Figure 3E). The corresponding AFM images showed mature fibrils of ~ 2.8 nm thickness and ~1.5 nm height (Figure 3E, inset). In the presence of Phe-BPM (**B1**) a dramatic augmentation of HuPrP aggregation was observed. At a 1:3 stoichiometric ratio, the lag phase reduced by more than 50% (12.2 h) and resulted in nearly 175% increase in ThT fluorescence (Figure 3A, Table 1). The acceleration was evident at all molar ratios, yielding aggregates with higher bulk and fibril thickness (~12 nm) compared to that of control fibers (Figures 3F). To rule out interference by the aromatic N-protecting group (-Z), a Boc-group was introduced (**B2**). Nevertheless, the aggregation kinetics remained majorly unperturbed with a lag phase matching closely to that of **B1** (Table 1, Supplementary Figure S28a).

Leu-BPMs delay prion polymerization

On replacing Phe with Leu (**B3**), a concentration dependent extension in the lag-phase was noted. The lag-phase became more prominent (~31 h) after replacing a single -Z with -Boc (**B4**), incurring significant loss in fluorescence maxima (~35% decrease; Table 1, Figures S28b & c). These observations suggested a correlation between hydrophobic residues and increase in lag phase. Building on these observations, we synthesized **B5** by replacing the -Z with -Boc group.

Interestingly, **B5** resulted in a strikingly prolonged lag phase at all molar ratios. A more than 60% increase in lag phase (~39 h) was observed at 1:3 molar ratio (Figure 3B, Table 1). The 60 h TEM and AFM images showed very thin fibrils stacking laterally to form bundles (~25 nm width; Figure 3G). We next investigated the combined effect of both Phe and Leu groups on amyloid formation by HuPrP. Interestingly, addition of **B6** (both Phe and Leu) reversed the delay effect exhibited by Leu-BPMs. This reversal (Figure 3C) not only enhanced the ThT binding but also resulted in lowering of the lag-phase (~12 h), comparable to that seen with Phe-BPMs (Table 1). The resulting

TEM and AFM images showed thick rod like assemblies (~32 nm width), probably resulting from lateral alignment of fibrils (Figure 3H).

Trp-BPMs abrogate prion polymerization

At this stage, we asked if an equally competent ring structure, not essentially constituting an aryl moiety may induce similar effects on HuPrP aggregation. The anticipation was justified by the hyperbolic ThT response of **B7** samples, indicating an accelerated HuPrP aggregation (Figure S28d, Table 1). Interestingly, on subsequent replacement of Z-group with -Boc (single, **B8**; both, **B9**), the sigmoidal ThT response was abrogated at all molar ratios (Figures S28e, Figure 3D). The effect was most prominent with **B9** that suppressed the ThT fluorescence to as low as ~5% of the control (Table 1). The corresponding TEM and AFM images of **B9** incubated samples taken after 60 h incubation showed depositions of amorphous aggregates of non-uniform sizes (Figures 3I). Overall the BPMs could expedite, delay or completely abolish HuPrP aggregation depending on their conjugated amino acids. It is important here to mention the role of protecting groups in maintaining the effect brought about by different BPMs. Our results clearly indicate that the presence of phenyl ring (either in form of conjugated side chain or as a protecting Z-group) can aid HuPrP fibrillation. While the role of aromatic protecting group (benzyloxy carbonyl or Z-group) cannot be ruled out, it was interesting to see how the subjugation in HuPrP aggregation by **B9** was lost when **B10** (no protecting groups) was added in the aggregating sample (Figure S28f, Table1).

BPMs specifically bind to HuPrP and alter its polymerization

Although all the BPMs significantly affected HuPrP amyloid aggregation, we proceeded with selective BPMs that displayed maximum modulatory effects (Supplementary Table T1). We analyzed each of these representative BPMs *i.e.* **B1** (acceleration), **B5** (delay), **B6** (reversal of delay by **B5**) and **B9** (inhibition) based on their characteristic effect on HuPrP aggregation (Figure S29). These different effects represent an interesting premise for exploring the actual molecular mechanisms affecting the nucleation-dependent conformational conversion of HuPrP. To confirm that the observed effects in HuPrP are specific and are fitting with our rationale of selecting the amino acid conjugates, we performed fluorescence binding experiments (Figure 4). We found that **B1**, **B5**, **B6** and **B9** bind to HuPrP with significant dissociation constants (K_d) ranging between 0.3-1.8 μM (Table 2). It was interesting to note that the amyloid inhibitory compound **B9** binds to HuPrP with highest affinity (K_d = 340 nM). Apart from this, we also tested the effect of BPM conjugated with a randomly selected amino acid lysine. The Lys-conjugated BPM **B11** upon incubation with HuPrP resulted in a ThT response similar to that of control HuPrP (Supplementary Figure S28g, Table 1). Thus, it is apparent that the alteration in the fibrillation process by Leu, Phe and Trp conjugated BPMs are amino acid specific and not a random phenomena.

Amyloid modulation by BPMs are specific to HuPrP

To document the specificity of the different BPMs, we further tested their effects on two other unrelated proteins *i.e.* α-synuclein and Islet amyloid polypeptide fragment ($IAPP_{20-29}$). While α-synuclein has been implicated in the pathogenesis of Parkinson's disease (PD), IAPP or amylin is responsible for islet amyloid formation in type 2 diabetes. The ThT fluorescence of aggregating α-synuclein, in the absence of any BPMs, followed a typical sigmoidal trend with a distinct lag phase of ~37 h (Figure S30, black traces). Addition of increasing molar equivalents of BPMs **B1**, **B5**, **B6** and **B9** did not significantly altered the aggregation kinetics. This was also evident from comparatively similar aggregation kinetics registered in all cases (Supplementary Table T1). Further, AFM images of aggregates showed morphologically similar amyloid fibers with average widths and heights of ~14 nm and ~9 nm respectively (Figure 5). On the other hand, $IAPP_{20-29}$ aggregation also showed a sigmoidal ThT response but was accompanied by a relatively shorter lag phase of ~8 h (Figure S31, black traces). Here also, addition of BPMs even at three times higher molar concentrations did not produce considerable change in ThT response. Although a decrease in lag phase in case of **B6** (6.6 h) and **B9** (7.1 h) was noted, but no significant change in

maximum ThT intensity was found. Similarly, no significant effect on the fibrillar morphology of the aggregates was found. The corresponding AFM images in each case showed large fibrillar architectures having average width of ~120 nm and height of ~80 nm (Figure 5). All these evidences suggested that BPMs modulate fibrillation in a prion specific manner and do not essentially alter the amyloid kinetics in these unrelated proteins.

BPMs influence prion oligomerization and secondary structural content of end-stage aggregates

To characterize BPM-modulated HuPrP aggregation at the molecular level, we monitored the particle size distribution in a time-wise manner using dynamic light scattering (DLS) (Figure S32). DLS pattern showed the presence of multiple species in each experimental system. However, since the major focus was to characterize the modulatory effects of different BPMs, averaged particle sizes were compared. This helped us in characterizing the effects of different BPMs (acceleration, delay or inhibition) and their ability to induce different type (sizes) of HuPrP aggregates. HuPrP alone formed aggregates with sizes more than 100 nm that appeared after 24 h incubation, marking the end of the lag-phase. Augmented aggregation state in **B1** and **B6** samples was evident by ~ 4.5 and ~ 2.5 fold higher aggregate dimensions at 24 h (Figure 6A). The appearance of higher order particle sizes in **B1** and **B6** (>1000 and 500 nm respectively) at the end of 48 h confirmed their acceleration effect on aggregation kinetics.

However, in case of **B5** and **B9**, a retarded progression in particle sizes ranging even lower than the control HuPrP aggregates was observed (<100 nm; 24 h). Interestingly, the particle sizes in **B9** samples remained consistently low even after 48 h affirming impediment in HuPrP self assembly process (magenta trace; Figure 6A).

Since amyloid aggregation involves substantial increase in β-sheet structures in aggregates, we next investigated the effect of BPMs on this structural transition. In our case, the observed morphological differences between the end-stage aggregates mediated by different BPMs led us to investigate their secondary structure contents. We characterized secondary structural signatures in each case using ATR-FTIR spectroscopy (Figure S33, S34, Supplementary Table T2) (65). A consistent β-sheet rich core (~45%) in HuPrP fibrils was evident due to the presence of cross-β (1622 cm^{-1}) and β-sheet peaks (1633 cm^{-1}) (Figure 6B). However, samples incubated with **B1** showed dramatic rise in the β-sheet content (~61%), supporting the presence of high fibrillar bulk and ThT response. On the contrary, β-sheet content in fibril-like aggregates induced by **B5** (~29%) was found significantly lower as compared to the control HuPrP fibrils. Besides, **B6** samples showed β-sheet content (~44%) similar to that of HuPrP. Interestingly, the non-fibrillar deposits induced by **B9** not only showed low β-sheet content (31%), but also the presence of more than 50% helical content. A relatively high helical content may be attributed to non-aggregated HuPrP monomers. Besides, it also indicates a delayed structural transformation that diverted away from the common β-sheet-rich fibrillar pathway. This was consistent with the accompanying abrogated ThT response in these samples. Thus, the non-fibrillar aggregates formed in the presence of **B9** indicated an *off-pathway* aggregation of HuPrP. Another very peculiar observation was the variation in β-turn contents in all aggregates. Compared to control HuPrP fibrils, **B5**-induced aggregates showed unusually high amounts of β-turns (~48%) which were dramatically reduced (~2%) in **B9**-induced aggregates (Supplementary Table T2).

BPMs alter morphological and toxic features of prion oligomers

Accumulating evidences indicate that small, soluble aggregates representing intermediates in the fibril assembly process are the primary toxic agents. These intermediates are categorized as amyloid oligomers that represent protein assemblies ranging from dimers to 24-mers, or even those of higher molecular weight (79, 80). The definition of oligomers varies and several types of natural and synthetically produced oligomers of different morphological features have been reported (81-83). In our report, we focus on oligomeric intermediates formed at the end of lag-phase during HuPrP aggregation. We utilized conformation-specific antibodies in combination

with AFM imaging to investigate whether the BPM-induced HuPrP oligomers also differ in their toxicities and morphologies. A11 antibodies generically recognize common epitopes present in the toxic oligomeric aggregates of amyloid proteins (84).

Since, the pre-fibrillar oligomers are known to be the most toxic species in any amyloid pathway, we chose to sample the oligomeric aggregates formed at the end of lag phase for each reaction. Owing to non observable lag phase, sampling in case of **B9** was done at 24 h to match the lag phase of HuPrP alone. Dot blot analysis of these aggregates with A11 antibodies showed significant differences in immunoreactivity (Figure 7A). The HuPrP oligomers alone and those induced by **B1** showed relatively similar binding to the A11 antibody. On the contrary, **B5** containing samples exhibited significantly increased immunoreactivity as compared to others indicating the presence of relatively higher proportions of toxic oligomeric species (Figure 7B). Interestingly, the A11 immunoreactivity remained unaltered in case of oligomeric aggregates of α-Synuclein formed either in presence or absence of different BPMs (Figure 7A and B).

We proceeded to probe if the differences in the pre-fibrillar oligomers towards A11 immunoreactivity are reflected as differences in their morphologies. AFM images of HuPrP oligomers showed species with an average width of 10-11 nm with heights ranging between 8-10 nm (Figure 7C). The **B1**-incubated samples showed ~4 fold larger (~40 nm) oligomers with radiating fibrillar appendages. In contrast, **B5** containing samples produced oligomers which were slightly smaller than HuPrP oligomers (~5-6 nm) with an average height of 6 nm. The high immunoreactivity of these oligomers corroborates their stabilization and delayed fibrillation. This is intriguing, since our observations differ remarkably with the previously reported stable oligomers of Aβ or delayed fibrillation in mouse prion that were obtained by following a mutational regime(46, 47, 85).

Interestingly, the **B6**-incubated samples showed large proto-filamentous structures (~40-45 nm), plausibly resulting from coalescence of oligomers. This indicated an altogether different mechanism of accelerated fibrillation as compared to that induced by **B1**. While in **B1**, the oligomers straightaway gave rise to fibrils, presence of **B6** accelerated the formation of pre-fibrillar aggregates. Besides, samples with **B9** showed the presence of large (~75-80 nm) and highly distended oligomers (Figure 7C). However, as observed in the AFM and TEM images, these oligomers failed to convert into fibrillar aggregates even after prolonged incubation (>60 h; Figure 3I). This is interesting, since BPMs by themselves do not assemble or aggregate at such low concentrations. Hence, the observed alterations in the oligomer morphology/sizes in presence of different BPMs indicate their specific interaction with HuPrP structure. This was reaffirmed when we observed no significant alterations in the oligomeric intermediates formed in case of α-Synuclein and $IAPP_{20-29}$. The α-Synuclein oligomers formed after 35 h incubation were large and roughly spherical with sizes ranging between 100-150 nm. The oligomers formed in presence of different BPMs also showed similar morphologies and dimensions (Figure S35). On the other hand, the $IAPP_{20-29}$ oligomers formed after 6 h incubation were also spherical in appearance but were significantly smaller in size (~12-16 nm). Here also, the oligomeric species remained unaffected even in presence of different BPMs and showed no change in morphological features (Figure S36). All these evidences indicate that BPMs interact with HuPrP structure in a specific manner and affect its fibrillation pathway as well as toxic features.

Remodeled HuPrP oligomers exhibit varied toxicities

Simoneau *et al* and other workers had previously shown that prion associated in *vitro* and in *vivo* toxicity is majorly attributed to its oligomeric form and not to the monomeric or fibrillar form (86, 87). Besides, the toxicity of oligomeric intermediates is reportedly brought about by their insidious interactions with cellular membranes (88). Hence, to establish that the differences in A11 immunoreactivity of oligomers also incurred differences in their actual toxicities, we tested their effect on cultured SH-SY5Y human neuroblastoma cells. The cells were treated with or without different oligomers and MTT reduction was monitored as a measure of cell viability (Figure 7D). Treatment with HuPrP oligomers

alone induced 50% reduction in cell viability after 24 h. Both **B1** and **B6** induced oligomers displayed toxicities marginally lower than HuPrP oligomers (~64% and ~ 55% respectively). Thus, in spite of accelerated aggregation kinetics, both **B1** and **B6** appear to follow *on-pathway* structural transitions and retain the toxic characteristics of HuPrP oligomers. This was in line with the A11 immunoreactivity data. However, **B5** induced oligomers were found severely toxic and resulted in just 20% cell viability. This confirmed that the B5 induced stabilized oligomers actually impregnated higher number of toxic epitopes. The observation is similar to engineered stabilization of Aβ oligomers that were relatively more toxic to neuronal cells than the normal oligomeric and pre-fibrillar species (85). Interestingly, **B9** mediated oligomers exhibited significant reduction in cell toxicity (viability>75%), suggesting that the large, distended oligomeric intermediates lacked major toxic elements. On the contrary, similar MTT reduction assay using α-Synuclein oligomers formed in absence and presence of different BPMs showed no considerable difference in neuronal toxicity (Figure 7D). This validates the unaltered A11 immunoreactivity and oligomer morphologies in presence of different BPMs described in previous sections. Overall, these experimental evidences are interesting, since none of the compounds showed cellular toxicity at their highest concentrations used in this study (Figure S37).

BPMs interact at critical α2-α3 helical interface of HuPrP

Global misfolding of prion protein incorporates a structural switch that systematically transforms the native PrP^{C} into a hyper-stable, pro-amyloid state or PrP^{Sc} (89). Our experimental observations indicate interference in this switch by BPMs, triggering a modified nucleation phenomenon. To obtain more molecular insights, we first performed molecular docking simulations. The most favorable binding poses of all BPMs were found at the interface of helix 2 (α2) and helix 3 (α3) of HuPrP (Figure S38). This interface encompasses the β2-α2 loop (residues 166-172) and the C-terminal part of the α3 helix (residues 218-231) (Figure 1A). On analyzing the 4 Å region of this binding pocket, it was found that hydrogen bonding and hydrophobic interactions were formed with common residues from β2-α2 loop and α3 helix *viz.* **B1** (Tyr 218, Gln 172), **B5** (Tyr 218, Gln 172, Arg 228), **B6** (Arg 164, Met 166, Arg 228), **B9** (Tyr 218, Gln 172, Arg 228) (Figure S38). Besides, the region in β2-α2 loop (169-YSNQNNF-175) owing to its mobility formed significant anchoring site that independently accommodated each BPM. Interestingly, H/D exchange experiments have shown that this interface actually forms the β-sheet core of human prion fibrils (90). Thus, the binding poses all together substantiate the experimental indications of BPM's interaction with secondary structural elements in HuPrP, leading to modifications in the aggregation pathway.

We further validated these observations by performing 125 ns explicit solvent MD simulations. A relatively higher backbone RMSD was registered for HuPrP in the absence as well as in the presence of **B1** or **B6** BPMs (Figure S39). This indicated the presence of perturbing structural elements in the native structure itself which were not influenced by the presence of either of these BPMs. However, the **B5** and **B9** complexes exhibited relatively low RMSD, indicating their stabilizing influence on HuPrP structure. To gain further insights, a comparative analysis of residue-wise RMSF was done (Figure 8, left panels). The results pointed towards two major structural elements of HuPrP in all complexes; one in the β2-α2 loop and the other at the α2-α3 loop (residues 190-200).

These results were in line with earlier report where structural rigidity of the β2-α2 loop aided by the low mobility of a conserved Tyr 169 residue prevents pathogenic conversion of prions (91). Conversely, fluctuation in this loop along with the Tyr 169 residue would facilitate amyloid conversion. This was evident in both **B1** and **B6** complexes where the loop flexibility overlapped with that of non-complexed HuPrP, indicating similar pro-aggregation states (left panels, Figure 8A and 8B). For **B5** complex, loop mobility was distributed over the entire β2-α2 loop (left panel, Figure 8C). Interestingly, the most remarkable reduction in Tyr 169 mobility was found in the case of **B9** complex (left panel, Figure 8D). With a concomitant reduction in the flexibility of the β2-α2 loop, the **B9** complexes were less likely to

undergo amyloid conversion, which was in congruence with our experimental observations.

The fluctuations of Tyr 169 are regulated by stabilizing contacts between Asp 178 (via H-bond) and Phe 175 (via π-π stacking) of the α2 helix (92). The Tyr 169-Phe 175 distances in the **B1** and **B6** complexes increased after 5 and 15 ns respectively, as compared to control, indicating a loss of π- π stacking (Supplementary Figure S40). On the contrary, a marked lowering of this distance in the **B9** complex indicated a rather stabilized Tyr conformation. Similar pattern was observed for the Tyr 169-Asp178 distances (Supplementary Figure S41). In **B1** and **B6** complexes this distance increased after 5 and 10 ns respectively, indicating breakage of H-bond. In **B5** and **B9** complexes however, this distance remained consistent throughout and almost overlapped with that of non-complexed HuPrP.

Together we concluded that the amyloid promoting effect of **B1** and **B6** is due to destabilization of π-π stacking and H-bonding interaction of Tyr 169. Earlier, prion oligomerization and fibrillation were shown to be influenced by structural elements of the α2 and α3-helices (93, 94). Unfolding of α2-α3 helices initiates amyloid aggregation in HuPrP. Consequently, restriction in the mobility of the connecting loop between these helices could be a mechanism to prevent amyloid-inducing deformations. Such was the case in **B1** and **B6** complexes where a reduction in mobility of α2-α3 loop was noted (left panels, Figures 7A, B). In contrast, **B5** and **B9** complexes showed comparatively low and no reduction in α2-α3 loop mobility respectively (left panels; Figure 8C, D).

BPMs affect the fold architecture of HuPrP

To determine how the loop flexibility influences the fold architecture of HuPrP in complex with different BPMs, we analyzed variations in the radius of gyrations (R_g). Radius of gyration for a protein defines the level of compaction in its structure *i.e.* the extent of folded or unfolded state of a polypeptide. The analysis of R_g of the entire protein showed maximum variation for the **B1** complex followed by **B6** (Figure S42). Relatively lower R_g variations were noted for **B5** and **B9** complexes, supporting their stabilizing effects. We extended our analysis to probe the R_g variations of α2 and α3 helices individually (Figure 8, middle and right panels). These helices are held together by a disulphide bond between Cys residues 179 and 214 in the native HuPrP structure (Figure 1A). In **B1** complex, R_g variations for both α2 and α3 helices were found marginally lower than that of HuPrP alone. However, transient changes involving helix-coil-helix transitions in both α2 and α3 near the disulphide linkage were observed (Figure 8A, middle and right panels respectively). In **B6** complex, R_g of α2 superposed with that of HuPrP alone (middle panel, Figure 8B). This was accompanied by transient unfolding near the disulphide linkage, similar to that observed in **B1** complex. At this stage, a dramatic increase in R_g of α3 was noted that corroborated with an unfolding transition observed near its C-terminus (black arrows, Figure 8B, right panel). This change persisted during the entire simulation period and was also corroborated by a significant increase in the solvent assessible surface area (Figure S43).

On the contrary, helix-coil-helix transitions were not observed in the **B5** and **B9** complexes (Figure 8C and 8D, middle and right panels respectively). The α3 helix in both these complexes showed stabilization due to the formation of extra helical components near the C-terminal end (black arrows, Figure 8C and 8D, right panels). Most importantly, the α2 helix in **B9** showed considerable lowering in R_g that was substantiated by an increase in helical component at the β2-α2 junction. Interestingly, β2-α2 loop in B9 complex also showed the formation of an helical component which may be attributed to the drastic reduction in loop mobility (black arrows, Figure 8C and 8D, middle panel). The stabilization effect was also corroborated by a significant loss in solvent assessible surface area (Supplementary Figure S44).

DISCUSSION

Few groups including ours have previously shown that π-π stacking essentially helps in making important contacts early in the aggregation pathway (64, 95). In contrast, several others have highlighted the role of high hydrophobicity and β-sheet propensities of aromatic residues in aiding structured aggregation (96, 97). In our report the accelerated kinetics observed in case of Phe-BPMs

(**B1** & **B2**) indicated escalation of favorable interactions directing ordered aggregation, plausibly due to early formation of critical nuclei. This underpins previous reports where aromatic interactions have been shown to play a deciding role in amyloid formation (98, 99). Moreover, induction of β-sheet transitions in prions are reportedly brought about by interactions of hydrophobic sites (100). Interestingly, Leu-BPMs (**B3**-**B5**) appear to alter hydrophobic interactions, plausibly leading to significant delay in the formation of critical nuclei. Thus, Phe and Leu in conjugation with the central bispidine scaffold implicated diametrically opposite effects on prion amyloidogenesis. Although both these BPMs induced fibrillation in HuPrP, the fiber morphologies as well as dye-binding abilities differed. Previously, replacement of Phe with Leu or Ala (aliphatic) has been shown to slow down the aggregation kinetics of Aβ and amylin (101, 102). However, these effects only implicated position specific roles of aromatic residues in short peptides. Our results with Phe- and Leu-BPMs suggest that structural features of the hydrophobic residues (aromatic or aliphatic) impart opposite effects on prion amyloidogenesis.

Further, it was equally interesting to find that aromaticity overshadows hydrophobicity when both Phe and Leu residues were co-conjugated as BPMs (**B6**). **B6** overturned prion aggregation with remarkable reduction in lag-phase, closely resembling Phe-BPMs. Although lateral alignment of fibrils was common in both **B5** (delayer) and **B6** (accelerator), relatively higher aggregate heights in **B6** (~40 nm) substantiated the augmented kinetics in presence of the latter. These variations imply different effects on packing of β-sheet building blocks and the way they stick together to form highly ordered amyloid structures. Our results thus indicate that aromatic interactions play critical role in transforming the early oligomeric and pre-fibrillar prion aggregates into end-stage fibrils. This notion was further validated when the aryl moiety was gradually replaced with an indole ring (TrP-BPMs) leading to complete inhibition of fibrillar pathway in HuPrP. These results corroborated that the large ring structure of Trp could entail steric hindrance to the amyloidogenic assembly of prions (103). Our results are in agreement with a recent report by Reymer *et al*. where heterogeneity in orientation and environment of aromatic residues was shown to define the variations in Sup35 prion strains (104). Due to their hydrophobic bispidine scaffold and specific amino acid residues, interaction between BPMs and HuPrP could hinder/facilitate HuPrP self-assembly and hence block/trigger amyloid aggregation. Thus, any structural variation in the end-stage aggregates (fibrillar or non-fibrillar) is attributed to these molecular specific interactions that affect initial nucleation of amyloid assembly. Importantly, these interactions are particular to HuPrP structural features and do not affect other unrelated proteins such as α-Synuclein and $IAPP_{20-29}$.

These observations favour our initial hypothesis where using aromatic and hydrophobic amino acids in the form of BPMs was proposed to influence amyloid formation of the protease resistant core of prion (90-231). A significant influence of ringed/aromatic protecting group (benzyloxy carbonyl or Z-group) in aiding fibrillation came from the observation that its presence, as seen in case of **B7** (two Z-groups), could mask the actual effect brought about by indole (TrP) side chains. In support, **B8** (1 Z-group) and **B9** (no Z-group) showed reduced and no masking, respectively. Besides, amyloid aggregation may also involve variety of other non-covalent interactions apart from hydrophobic and aromatic interactions (105). This may be tested in future where all the 20 different amino acids are conjugated in various combinations and used to understand their amyloid modulatory effect.

In an un-interrupted amyloid aggregation, end of lag-phase is characterized by rapid oligomeric associations that determine the structural features of the final fibrillar forms (106). These oligomeric intermediates are pathological hallmarks of prions as well as several other amyloid proteins such as Aβ and α-synuclein (107). In our case, the **B5** induced oligomers resembled the stable neurotoxic Alzheimer's associated amyloid-β oligomers reported by Sandberg *et al* (85). We argued that **B5** induced formation of oligomeric intermediates that have relatively lower tendency to convert into fibrillar assemblies. Nevertheless, both **B1** and **B6** induced oligomers resembled untreated HuPrP oligomers in their A11 immunoreactivity, indicating lesser number of toxic epitopes as compared to **B5**.

Interestingly, **B9** incubated samples showed least immunoreactivity, suggesting loss of toxic epitopes during the remodeling process. Their low immunoreactivity could be attributed either to an altered assembly of oligomers or to an advanced or receded state of aggregation.

Formation of fibrillar appendages in **B1** induced oligomers reinforced that higher order fibrillar aggregates appear early in these samples. This also correlates with the augmented aggregation kinetics in **B1** containing samples as oligomers appear to directly convert to fibrils by skipping the pre-fibrillar or protofilament stage. In contrast, **B5** containing samples produced oligomers which were slightly smaller than HuPrP oligomers (~5-6 nm) with an average height of 6 nm (Figure 7C). This structural alteration along with the observed high A11 immunoreactivity corroborates stabilization and delayed fibrillation capabilities of **B5**-induced oligomers. This is intriguing, since our observations differ remarkably with the previously reported stable oligomers of Aβ or delayed fibrillation in mouse prion that were obtained by following a mutational regime (46, 47, 85). Furthermore, the **B6** induced oligomeric intermediates resembled beaded assembly of oligomers fusing together to form higher order aggregates. This again implied a remodeled amyloidogenic pathway that favors quicker assembly of oligomers into proto-fibrillar ensembles. Equally interesting observation was the formation of large and distended oligomeric structures in **B9** samples. Apparently, these large oligomers were energetically disfavored that collapsed later and receded into unordered aggregates with time (Fig.1I). Formation of these unordered aggregates indicates an *off-pathway* modulation, similar to the effect of resveratrol and cyclic KLVFF-derived peptide on Aβ amyloidogenesis (76, 108). PrP^{Sc} reportedly exists in an oligomeric and membrane-associated form and its accumulation compromises fundamental membrane functions (8). Hence, the variation in toxicities between the BPM-induced HuPrP oligomers could be due to conformational differences between them which significantly alter their membrane interactions.

In our case, the oligomeric toxicities correlated well with the secondary structural contents of BPM-induced end stage aggregates. **B5** induces the formation of highly toxic, small oligomeric intermediates that slowly transform into fibrillar aggregates rich in β-turn content. On the contrary, presence of **B9** resulted in oligomers with significantly reduced toxicity that later form unstructured aggregates with very low β-turn content. Also, β-turn formation involves interactions that are largely local and may thus affect fibril nucleation and equilibrium (109). Previously, nucleation by the formation of β-turn had been shown to be a rate-limiting step in oligomer stabilization (110). Further, the aggregates having β-sheet content higher (**B1**) or similar (**B6**) to HuPrP were preceded by oligomers with cellular toxicities resembling HuPrP oligomers. Thus, a remarkable maneuver of β-sheet and β-turn content in deciding the fate and characteristics of prion oligomeric assemblies is discernible. The variation in β-sheet and β-turn contents and their contribution to prion polymerization behavior in this context is particularly noticeable. While a high β-sheet content (HuPrP alone and in presence of **B1**) directs an *on-pathway* fibril nucleation pathway, peculiar alterations are observed with increasing β-turn content (**B5** and **B6**). Importantly, significantly low β-sheet content leads to an *off-pathway*, non-fibrillar remodeling process (**B9**). Moreover, the toxicities of oligomers are likely to vary depending on whether the nucleation leads to intermediates that are '*on*' or '*off*' *pathway*.

Earlier, prion oligomerization and fibrillation were shown to be influenced by structural elements of the α2 and α3-helices (93, 94). Unfolding of α2-α3 helices initiates amyloid aggregation in HuPrP. Consequently, restriction in the mobility of the connecting loop between these helices could be a mechanism to prevent amyloid-inducing deformations. The MD simulation results corroborated this notion where a reduction in mobility of the α2-α3 loop was noted in both **B1** and **B6** complexes (left panels, Figure 7A, B). In contrast, **B5** and **B9** complexes showed comparatively low and no reduction in the α2-α3 loop mobility, respectively (left panels; Figure 8C, D). Furthermore, augmentation of prion polymerization by both **B1** and **B6** are attributed to destabilization of π-π stacking and H-bonding interaction of Tyr 169 residue. In effect, the entire β2-α2 loop region (169-YSNQNNF-175) has been shown to possess local conformational

polymorphism and undergoes transition between 3_{10}-helix and β turn, when the Tyr 169 is mutated (111, 112). The Tyr 169 moiety is strictly conserved in mammalian prions and its mobility is shown to affect the mobility of the entire loop. Higher β2-α2 loop mobility is implicated as a principle cause of prion conversion and transmission in *vivo* (91, 113). Additionally, the heptapeptide segment 169-YSNQNNF-175 shares high sequence similarity to GNNQQNY heptapeptide from the yeast prion protein Sup35 that forms steric zipper fibrils (114).

Our results strongly suggest that the differential effects of BPMs are mediated by perturbation or stabilization of both local and global structural components of HuPrP. It is evident that the presence of both the accelerators **B1** and **B6** resulted in destabilizing helix-coil-helix transitions in the α2 and α3 helices of HuPrP leaving the β2-α2 loop mostly unaffected. A relatively higher degree of R_g variation noted for the **B1** complex indicated that in this case, besides the α2-α3 helices, stability of the entire protein is altered. Both these outcomes explain the observed dissimilarities in amyloid acceleration mechanisms by these BPMs. On the other hand, the delayer **B5** and the inhibitor **B9** containing complexes mostly stabilized the α2 and α3 helices by inducing extra helical contents. However, the mobility of β2-α2 loop could be considered a crucial factor that determined delay and inhibitory effect by **B5** and **B9**, respectively.

In light of the above experimental and theoretical evidences, it is construed that BPMs affect different steps of supramolecular prion polymerization pathway. The significantly high binding free energy changes noted for BPMs **B1**, **B5**, **B6** and **B9** (Table 2) indicated that they specifically bind to HuPrP and alter its polymerization by affecting the energy barriers associated with its fibrillation pathway. Perhaps, **B1** augments amyloid formation by lowering the energy barrier of fibrillation and induces direct conversion to fibrillar state by skipping intermediate states (Figure 9, red trace). On the other hand, **B5** induces the formation of stable oligomers by trapping them into an intermediate state that delays the formation of critical nuclei (Figure 9, green trace). **B6** reverses this delay, by lowering the energy barrier for conversion of oligomers to protofilaments (Figure 9, blue trace). On the contrary, **B9** influenced aggregation bypasses the canonical prion nucleation pathway and proceeds via an *off-pathway* oligomerization step (Figure 9, magenta trace). This leads to the formation of energetically disfavored, large oligomers that finally collapse into unstructured aggregates. Further, molecular details of these BPM mediated alterations as well as their applicability in controlling other nucleation-dependent supramolecular polymerizations remains to be seen.

Our results entail differential roles of aromatic and hydrophobic interactions in achieving an *on-pathway* or *off-pathway* aggregation in HuPrP. The resulting differences in HuPrP aggregation kinetics, oligomeric and end-stage morphology in the presence of BPMs entail alterations in these favorable non-covalent interactions. We show that the amyloid specific conformational rearrangements in prion protein can be effectively influenced by synthetic scaffolds conjugating hydrophobic/aromatic side chains. In conclusion, BPMs modulate prion polymerization by forming discrete oligomeric nanostructures that differ in sizes, toxic properties, end-stage fibril morphology and secondary structural signatures. We thus propose BPMs as excellent candidates for altering the aggregation of amyloidogenic proteins and may hold potential therapeutic utility.

ACKNOWLEDGEMENTS

The authors thank the Indian Institute of Technology Delhi (IIT Delhi) and National Institute of Immunology (NII) for infrastructural support. A.S., S.S., S.S. and J.S. acknowledge scholarship support from ICMR, UGC, DST & CSIR and IIT Delhi, respectively. The authors acknowledge Dr. Pramit Chowdhury, IIT Delhi for providing us recombinant α-Synuclein protein. The authors are indebted to Dr. Deepak Dasgupta, SINP Kolkata and Dr. Saurabh Gautam, IIT Delhi for technical discussions. The authors also thank the Department of Biotechnology, Govt. of India, for funding.

AUTHOR CONTRIBUTION

VH and BK conceived and coordinated the study. AS designed, performed and analyzed the experiments. SS1 and SS2 designed and synthesized the compounds and performed the experiments. SG1 and SG2 performed

and analyzed the cell culture experiments. AS and JS did the computational work. AS, VH and BK wrote the manuscript. All authors analyzed the results and approved the final version of the manuscript.

REFERENCES

1. Whitesides GM, Mathias JP, Seto CT. Molecular self-assembly and nanochemistry: a chemical strategy for the synthesis of nanostructures. Science. 1991;254(5036):1312-9.
2. Knowles TPJ, Vendruscolo M, Dobson CM. The amyloid state and its association with protein misfolding diseases. Nat Rev Mol Cell Bio. 2014;15(6):384-96.
3. Aguzzi A, Sigurdson C, Heikenwaelder M. Molecular mechanisms of prion pathogenesis. Annu Rev Pathol-Mech. 2008;3:11-40.
4. Stohr J, Weinmann N, Wille H, Kaimann T, Nagel-Steger L, Birkmann E, et al. Mechanisms of prion protein assembly into amyloid. Proceedings of the National Academy of Sciences of the United States of America. 2008;105(7):2409-14.
5. Kovacs GG, Budka H. Prion diseases: from protein to cell pathology. The American journal of pathology. 2008;172(3):555-65.
6. Imran M, Mahmood S. An overview of human prion diseases. Virology journal. 2011;8:559.
7. Kundu B, Maiti NR, Jones EM, Surewicz KA, Vanik DL, Surewicz WK. Nucleation-dependent conformational conversion of the Y145Stop variant of human prion protein: structural clues for prion propagation. Proceedings of the National Academy of Sciences of the United States of America. 2003;100(21):12069-74.
8. Caughey B, Baron GS, Chesebro B, Jeffrey M. Getting a Grip on Prions: Oligomers, Amyloids, and Pathological Membrane Interactions. Annu Rev Biochem. 2009;78:177-204.
9. Collins SR, Douglass A, Vale RD, Weissman JS. Mechanism of prion propagation: amyloid growth occurs by monomer addition. PLoS biology. 2004;2(10):e321.
10. Yu H, Liu X, Neupane K, Gupta AN, Brigley AM, Solanki A, et al. Direct observation of multiple misfolding pathways in a single prion protein molecule. Proceedings of the National Academy of Sciences of the United States of America. 2012;109(14):5283-8.
11. Cho KR, Huang Y, Yu SL, Yin SM, Plomp M, Qiu SR, et al. A Multistage Pathway for Human Prion Protein Aggregation in Vitro: From Multimeric Seeds to beta-Oligomers and Nonfibrillar Structures. J Am Chem Soc. 2011;133(22):8586-93.
12. Zhu L, Song Y, Cheng PN, Moore JS. Molecular Design for Dual Modulation Effect of Amyloid Protein Aggregation. J Am Chem Soc. 2015;137(25):8062-8.
13. Ferrao-Gonzales AD, Robbs BK, Moreau VH, Ferreira A, Juliano L, Valente AP, et al. Controlling {beta}-amyloid oligomerization by the use of naphthalene sulfonates: trapping low molecular weight oligomeric species. The Journal of biological chemistry. 2005;280(41):34747-54.
14. Du WJ, Guo JJ, Gao MT, Hu SQ, Dong XY, Han YF, et al. Brazilin inhibits amyloid beta-protein fibrillogenesis, remodels amyloid fibrils and reduces amyloid cytotoxicity. Scientific reports. 2015;5:7992.
15. Bieschke J, Herbst M, Wiglenda T, Friedrich RP, Boeddrich A, Schiele F, et al. Small-molecule conversion of toxic oligomers to nontoxic beta-sheet-rich amyloid fibrils. Nature chemical biology. 2012;8(1):93-101.
16. Bulic B, Pickhardt M, Khlistunova I, Biernat J, Mandelkow EM, Mandelkow E, et al. Rhodanine-based tau aggregation inhibitors in cell models of tauopathy. Angewandte Chemie. 2007;46(48):9215-9.
17. Srivastava A, Arya P, Goel S, Kundu B, Mishra P, Fnu A. Gelsolin Amyloidogenesis Is Effectively Modulated by Curcumin and Emetine Conjugated PLGA Nanoparticles. Plos One. 2015;10(5):e0127011.
18. Peterson SA, Klabunde T, Lashuel HA, Purkey H, Sacchettini JC, Kelly JW. Inhibiting transthyretin conformational changes that lead to amyloid fibril formation. Proceedings of the National Academy of Sciences of the United States of America. 1998;95(22):12956-60.

19. Ma B, Nussinov R. The stability of monomeric intermediates controls amyloid formation: Abeta25-35 and its N27Q mutant. Biophys J. 2006;90(10):3365-74.
20. Poduslo JF, Curran GL, Kumar A, Frangione B, Soto C. Beta-sheet breaker peptide inhibitor of Alzheimer's amyloidogenesis with increased blood-brain barrier permeability and resistance to proteolytic degradation in plasma. Journal of neurobiology. 1999;39(3):371-82.
21. Muchowski PJ, Wacker JL. Modulation of neurodegeneration by molecular chaperones. Nature reviews Neuroscience. 2005;6(1):11-22.
22. Tomar R, Garg DK, Mishra R, Thakur AK, Kundu B. N-terminal domain of Pyrococcus furiosus l-asparaginase functions as a non-specific, stable, molecular chaperone. The FEBS journal. 2013;280(11):2688-99.
23. Cohen FE, Kelly JW. Therapeutic approaches to protein-misfolding diseases. Nature. 2003;426(6968):905-9.
24. Martins PM. True and apparent inhibition of amyloid fibril formation. Prion. 2013;7(2):136-9.
25. Salloway S, Sperling R, Fox NC, Blennow K, Klunk W, Raskind M, et al. Two phase 3 trials of bapineuzumab in mild-to-moderate Alzheimer's disease. The New England journal of medicine. 2014;370(4):322-33.
26. Wang H, Raleigh DP. General Amyloid Inhibitors? A Critical Examination of the Inhibition of IAPP Amyloid Formation by Inositol Stereoisomers. Plos One. 2014;9(9).
27. Perez DR, Damberger FF, Wuthrich K. Horse Prion Protein NMR Structure and Comparisons with Related Variants of the Mouse Prion Protein (vol 400, pg 121, 2010). J Mol Biol. 2010;402(5):929-30.
28. Wen Y, Li J, Yao WM, Xiong MQ, Hong J, Peng Y, et al. Unique Structural Characteristics of the Rabbit Prion Protein. J Biol Chem. 2010;285(41):31682-93.
29. Zhou Z, Yan X, Pan K, Chen J, Xie ZS, Xiao GF, et al. Fibril Formation of the Rabbit/Human/Bovine Prion Proteins. Biophys J. 2011;101(6):1483-92.
30. Pastore A, Zagari A. A structural overview of the vertebrate prion proteins. Prion. 2007;1(3):185-97.
31. Saverioni D, Notari S, Capellari S, Poggiolini I, Giese A, Kretzschmar HA, et al. Analyses of protease resistance and aggregation state of abnormal prion protein across the spectrum of human prions. The Journal of biological chemistry. 2013;288(39):27972-85.
32. Baron T, Crozet C, Biacabe AG, Philippe S, Verchere J, Bencsik A, et al. Molecular analysis of the protease-resistant prion protein in scrapie and bovine spongiform encephalopathy transmitted to ovine transgenic and wild-type mice. J Virol. 2004;78(12):6243-51.
33. Safar J, Wille H, Itri V, Groth D, Serban H, Torchia M, et al. Eight prion strains have PrP(Sc) molecules with different conformations. Nat Med. 1998;4(10):1157-65.
34. Yamaguchi K, Kamatari YO, Fukuoka M, Miyaji R, Kuwata K. Nearly Reversible Conformational Change of Amyloid Fibrils as Revealed by pH-Jump Experiments. Biochemistry. 2013;52(39):6797-806.
35. Thellung S, Gatta E, Pellistri F, Corsaro A, Villa V, Vassalli M, et al. Excitotoxicity Through NMDA Receptors Mediates Cerebellar Granule Neuron Apoptosis Induced by Prion Protein 90-231 Fragment. Neurotox Res. 2013;23(4):301-14.
36. Chen SG, Teplow DB, Parchi P, Teller JK, Gambetti P, Autiliogambetti L. Truncated Forms of the Human Prion Protein in Normal Brain and in Prion Diseases. J Biol Chem. 1995;270(32):19173-80.
37. Khan MQ, Sweeting B, Mulligan VK, Arslan PE, Cashman NR, Pai EF, et al. Prion disease susceptibility is affected by beta-structure folding propensity and local side-chain interactions in PrP. Proceedings of the National Academy of Sciences of the United States of America. 2010;107(46):19808-13.
38. Martinez J, Sanchez R, Castellanos M, Makarava N, Aguzzi A, Baskakov IV, et al. PrP charge structure encodes interdomain interactions. Scientific reports. 2015;5.

39. Yu H, Dee DR, Liu X, Brigley AM, Sosova I, Woodside MT. Protein misfolding occurs by slow diffusion across multiple barriers in a rough energy landscape. Proceedings of the National Academy of Sciences of the United States of America. 2015;112(27):8308-13.
40. Concha-Marambio L, Diaz-Espinoza R, Soto C. The Extent of Protease Resistance of Misfolded Prion Protein Is Highly Dependent on the Salt Concentration. J Biol Chem. 2014;289(5):3073-9.
41. Apetri AC, Vanik DL, Surewicz WK. Polymorphism at residue 129 modulates the conformational conversion of the D178N variant of human prion protein 90-231. Biochemistry. 2005;44(48):15880-8.
42. Wille H, Michelitsch MD, Guenebaut V, Supattapone S, Serban A, Cohen FE, et al. Structural studies of the scrapie prion protein by electron crystallography. Proceedings of the National Academy of Sciences of the United States of America. 2002;99(6):3563-8.
43. Govaerts C, Wille H, Prusiner SB, Cohen FE. Evidence for assembly of prions with left-handed beta-helices into trimers. Proceedings of the National Academy of Sciences of the United States of America. 2004;101(22):8342-7.
44. Dima RI, Thirumalai D. Exploring the propensities of helices in PrP(C) to form beta sheet using NMR structures and sequence alignments. Biophys J. 2002;83(3):1268-80.
45. Dima RI, Thirumalai D. Probing the instabilities in the dynamics of helical fragments from mouse PrPC. Proceedings of the National Academy of Sciences of the United States of America. 2004;101(43):15335-40.
46. Kong Q, Mills JL, Kundu B, Li X, Qing L, Surewicz K, et al. Thermodynamic stabilization of the folded domain of prion protein inhibits prion infection in vivo. Cell reports. 2013;4(2):248-54.
47. Singh J, Kumar H, Sabareesan AT, Udgaonkar JB. Rational Stabilization of Helix 2 of the Prion Protein Prevents Its Misfolding and Oligomerization. J Am Chem Soc. 2014;136(48):16704-7.
48. Fitzmaurice TJ, Burke DF, Hopkins L, Yang S, Yu S, Sy MS, et al. The stability and aggregation of ovine prion protein associated with classical and atypical scrapie correlates with the ease of unwinding of helix-2. The Biochemical journal. 2008;409(2):367-75.
49. Gazit E. Global analysis of tandem aromatic octapeptide repeats: the significance of the aromatic-glycine motif. Bioinformatics. 2002;18(6):880-3.
50. Coleman BM, Harrison CF, Guo B, Masters CL, Barnham KJ, Lawson VA, et al. Pathogenic Mutations within the Hydrophobic Domain of the Prion Protein Lead to the Formation of Protease-Sensitive Prion Species with Increased Lethality. J Virol. 2014;88(5):2690-703.
51. Wasmer C, Lange A, Van Melckebeke H, Siemer AB, Riek R, Meier BH. Amyloid fibrils of the HET-s(218-289) prion form a beta solenoid with a triangular hydrophobic core. Science. 2008;319(5869):1523-6.
52. Scorciapino MA, Rinaldi AC. Antimicrobial peptidomimetics: reinterpreting nature to deliver innovative therapeutics. Frontiers in immunology. 2012;3:171.
53. Whitby LR, Boger DL. Comprehensive peptidomimetic libraries targeting protein-protein interactions. Accounts of chemical research. 2012;45(10):1698-709.
54. Vagner J, Qu H, Hruby VJ. Peptidomimetics, a synthetic tool of drug discovery. Current opinion in chemical biology. 2008;12(3):292-6.
55. Akram ON, DeGraff DJ, Sheehan JH, Tilley WD, Matusik RJ, Ahn JM, et al. Tailoring peptidomimetics for targeting protein-protein interactions. Molecular cancer research : MCR. 2014;12(7):967-78.
56. Haridas V, Sadanandan S, Gopalakrishna MVS, Bijesh MB, Verma RP, Chinthalapalli S, et al. Bispidine as a helix inducing scaffold: examples of helically folded linear peptides. Chem Commun. 2013;49(93):10980-2.
57. Haridas V, Sadanandan S, Sharma YK, Chinthalapalli S, Shandilya A. Bispidine as a secondary structure nucleator in peptides. Tetrahedron Lett. 2012;53(6):623-6.
58. Zahn R, von Schroetter C, Wuthrich K. Human prion proteins expressed in Escherichia coli and purified by high-affinity column refolding. FEBS letters. 1997;417(3):400-4.

59. Gautam S, Karmakar S, Bose A, Chowdhury PK. beta-cyclodextrin and curcumin, a potent cocktail for disaggregating and/or inhibiting amyloids: a case study with alpha-synuclein. Biochemistry. 2014;53(25):4081-3.
60. Cobb NJ, Apetri AC, Surewicz WK. Prion Protein Amyloid Formation under Native-like Conditions Involves Refolding of the C-terminal alpha-Helical Domain. J Biol Chem. 2008;283(50):34704-11.
61. van Maarschalkerweerd A, Vetri V, Langkilde AE, Fodera V, Vestergaard B. Protein/lipid coaggregates are formed during alpha-synuclein-induced disruption of lipid bilayers. Biomacromolecules. 2014;15(10):3643-54.
62. Cabaleiro-Lago C, Lynch I, Dawson KA, Linse S. Inhibition of IAPP and IAPP(20-29) fibrillation by polymeric nanoparticles. Langmuir : the ACS journal of surfaces and colloids. 2010;26(5):3453-61.
63. Uversky VN, Li J, Fink AL. Metal-triggered structural transformations, aggregation, and fibrillation of human alpha-synuclein. A possible molecular NK between Parkinson's disease and heavy metal exposure. The Journal of biological chemistry. 2001;276(47):44284-96.
64. Arya P, Srivastava A, Vasaikar SV, Mukherjee G, Mishra P, Kundu B. Selective Interception of Gelsolin Amyloidogenic Stretch Results in Conformationally Distinct Aggregates with Reduced Toxicity. Acs Chem Neurosci. 2014;5(10):982-92.
65. Ridgley DM, Ebanks KC, Barone JR. Peptide Mixtures Can Self-Assemble into Large Amyloid Fibers of Varying Size and Morphology. Biomacromolecules. 2011;12(10):3770-9.
66. Ilc G, Giachin G, Jaremko M, Jaremko L, Benetti F, Plavec J, et al. NMR Structure of the Human Prion Protein with the Pathological Q212P Mutation Reveals Unique Structural Features. Plos One. 2010;5(7).
67. Schuttelkopf AW, van Aalten DM. PRODRG: a tool for high-throughput crystallography of protein-ligand complexes. Acta crystallographica Section D, Biological crystallography. 2004;60(Pt 8):1355-63.
68. Lee HS, Zhang Y. BSP-SLIM: A blind low-resolution ligand-protein docking approach using predicted protein structures. Proteins. 2012;80(1):93-110.
69. Mills JEJ, Dean PM. Three-dimensional hydrogen-bond geometry and probability information from a crystal survey. J Comput Aid Mol Des. 1996;10(6):607-22.
70. Pronk S, Pall S, Schulz R, Larsson P, Bjelkmar P, Apostolov R, et al. GROMACS 4.5: a high-throughput and highly parallel open source molecular simulation toolkit. Bioinformatics. 2013;29(7):845-54.
71. Zoete V, Cuendet MA, Grosdidier A, Michielin O. SwissParam: A Fast Force Field Generation Tool for Small Organic Molecules. J Comput Chem. 2011;32(11):2359-68.
72. Jorgensen WL, Chandrasekhar J, Madura JD, Impey RW, Klein ML. Comparison of Simple Potential Functions for Simulating Liquid Water. Journal of Chemical Physics. 1983;79(2):926-35.
73. Linse B, Linse P. Tuning the smooth particle mesh Ewald sum: application on ionic solutions and dipolar fluids. The Journal of chemical physics. 2014;141(18):184114.
74. Slovak J, Tanaka H. Computer simulation study of metastable ice VII and amorphous phases obtained by its melting. The Journal of chemical physics. 2005;122(20):204512.
75. Biancalana M, Koide S. Molecular mechanism of Thioflavin-T binding to amyloid fibrils. Biochimica et biophysica acta. 2010;1804(7):1405-12.
76. Ladiwala AR, Lin JC, Bale SS, Marcelino-Cruz AM, Bhattacharya M, Dordick JS, et al. Resveratrol selectively remodels soluble oligomers and fibrils of amyloid Abeta into off-pathway conformers. The Journal of biological chemistry. 2010;285(31):24228-37.
77. Arosio P, Knowles TP, Linse S. On the lag phase in amyloid fibril formation. Physical chemistry chemical physics : PCCP. 2015;17(12):7606-18.
78. Masel J, Jansen VAA, Nowak MA. Quantifying the kinetic parameters of prion replication. Biophys Chem. 1999;77(2-3):139-52.

79. Sakono M, Zako T. Amyloid oligomers: formation and toxicity of Abeta oligomers. The FEBS journal. 2010;277(6):1348-58.
80. Fandrich M. Oligomeric Intermediates in Amyloid Formation: Structure Determination and Mechanisms of Toxicity. J Mol Biol. 2012;421(4-5):427-40.
81. Liu P, Paulson JB, Forster CL, Shapiro SL, Ashe KH, Zahs KR. Characterization of a Novel Mouse Model of Alzheimer's Disease--Amyloid Pathology and Unique beta-Amyloid Oligomer Profile. Plos One. 2015;10(5):e0126317.
82. Huang P, Lian F, Wen Y, Guo C, Lin D. Prion protein oligomer and its neurotoxicity. Acta biochimica et biophysica Sinica. 2013;45(6):442-51.
83. Balducci C, Beeg M, Stravalaci M, Bastone A, Sclip A, Biasini E, et al. Synthetic amyloid-beta oligomers impair long-term memory independently of cellular prion protein. Proceedings of the National Academy of Sciences of the United States of America. 2010;107(5):2295-300.
84. Kayed R, Head E, Thompson JL, McIntire TM, Milton SC, Cotman CW, et al. Common structure of soluble amyloid oligomers implies common mechanism of pathogenesis. Science. 2003;300(5618):486-9.
85. Sandberg A, Luheshi LM, Sollvander S, de Barros TP, Macao B, Knowles TPJ, et al. Stabilization of neurotoxic Alzheimer amyloid-beta oligomers by protein engineering. Proceedings of the National Academy of Sciences of the United States of America. 2010;107(35):15595-600.
86. Simoneau S, Rezaei H, Sales N, Kaiser-Schulz G, Lefebvre-Roque M, Vidal C, et al. In vitro and in vivo neurotoxicity of prion protein oligomers. PLoS pathogens. 2007;3(8):e125.
87. Sasaki K, Minaki H, Iwaki T. Development of oligomeric prion-protein aggregates in a mouse model of prion disease. J Pathol. 2009;219(1):123-30.
88. Jang H, Connelly L, Arce FT, Ramachandran S, Kagan BL, Lal R, et al. Mechanisms for the Insertion of Toxic, Fibril-like beta-Amyloid Oligomers into the Membrane. J Chem Theory Comput. 2013;9(1):822-33.
89. Gerber R, Tahiri-Alaoui A, Hore PJ, James W. Conformational pH dependence of intermediate states during oligomerization of the human prion protein. Protein Sci. 2008;17(3):537-44.
90. Lu X, Wintrode PL, Surewicz WK. Beta-sheet core of human prion protein amyloid fibrils as determined by hydrogen/deuterium exchange. Proceedings of the National Academy of Sciences of the United States of America. 2007;104(5):1510-5.
91. Kurt TD, Jiang L, Bett C, Eisenberg D, Sigurdson CJ. A proposed mechanism for the promotion of prion conversion involving a strictly conserved tyrosine residue in the beta2-alpha2 loop of PrPC. The Journal of biological chemistry. 2014;289(15):10660-7.
92. Gorfe AA, Caflisch A. Ser170 controls the conformational multiplicity of the loop 166-175 in prion proteins: implication for conversion and species barrier. Faseb J. 2007;21(12):3279-87.
93. Chakroun N, Prigent S, Dreiss CA, Noinville S, Chapuis C, Fraternali F, et al. The oligomerization properties of prion protein are restricted to the H2H3 domain. Faseb J. 2010;24(9):3222-31.
94. Adrover M, Pauwels K, Prigent S, de Chiara C, Xu Z, Chapuis C, et al. Prion Fibrillization Is Mediated by a Native Structural Element That Comprises Helices H2 and H3. J Biol Chem. 2010;285(27):21004-12.
95. Gsponer J, Haberthur U, Caflisch A. The role of side-chain interactions in the early steps of aggregation: Molecular dynamics simulations of an amyloid-forming peptide from the yeast prion Sup35. Proceedings of the National Academy of Sciences of the United States of America. 2003;100(9):5154-9.
96. Bemporad F, Taddei N, Stefani M, Chiti F. Assessing the role of aromatic residues in the amyloid aggregation of human muscle acylphosphatase. Protein Sci. 2006;15(4):862-70.
97. Doran TM, Kamens AJ, Byrnes NK, Nilsson BL. Role of amino acid hydrophobicity, aromaticity, and molecular volume on IAPP(20-29) amyloid self-assembly. Proteins. 2012;80(4):1053-65.
98. Gazit E. A possible role for pi-stacking in the self-assembly of amyloid fibrils. Faseb J. 2002;16(1):77-83.

99. Tu LH, Raleigh D. Analysis of the Role of Aromatic Interactions in Amyloid Formation by Islet Amyloid Polypeptide. Biophys J. 2013;104(2):47a-a.
100. Leffers KW, Schell J, Jansen K, Lucassen R, Kaimann T, Nagel-Steger L, et al. The structural transition of the prion protein into its pathogenic conformation is induced by unmasking hydrophobic sites. J Mol Biol. 2004;344(3):839-53.
101. Cukalevski R, Boland B, Frohm B, Thulin E, Walsh D, Linse S. Role of Aromatic Side Chains in Amyloid beta-Protein Aggregation. Acs Chem Neurosci. 2012;3(12):1008-16.
102. Azriel R, Gazit E. Analysis of the minimal amyloid-forming fragment of the islet amyloid polypeptide. An experimental support for the key role of the phenylalanine residue in amyloid formation. The Journal of biological chemistry. 2001;276(36):34156-61.
103. Sabate R, Rousseau F, Schymkowitz J, Ventura S. What Makes a Protein Sequence a Prion? Plos Comput Biol. 2015;11(1).
104. Reymer A, Frederick KK, Rocha S, Beke-Somfai T, Kitts CC, Lindquist S, et al. Orientation of aromatic residues in amyloid cores: structural insights into prion fiber diversity. Proceedings of the National Academy of Sciences of the United States of America. 2014;111(48):17158-63.
105. Marshall KE, Morris KL, Charlton D, O'Reilly N, Lewis L, Walden H, et al. Hydrophobic, aromatic, and electrostatic interactions play a central role in amyloid fibril formation and stability. Biochemistry. 2011;50(12):2061-71.
106. Serio TR, Cashikar AG, Kowal AS, Sawicki GJ, Moslehi JJ, Serpell L, et al. Nucleated conformational conversion and the replication of conformational information by a prion determinant. Science. 2000;289(5483):1317-21.
107. Ferreira ST, Vieira MNN, De Felice FG. Soluble protein oligomers as emerging toxins in Alzheimer's and other amyloid diseases. Iubmb Life. 2007;59(4-5):332-45.
108. Arai T, Sasaki D, Araya T, Sato T, Sohma Y, Kanai M. A cyclic KLVFF-derived peptide aggregation inhibitor induces the formation of less-toxic off-pathway amyloid-beta oligomers. Chembiochem : a European journal of chemical biology. 2014;15(17):2577-83.
109. Marcelino AMC, Gierasch LM. Roles of beta-turns in protein folding: From peptide models to protein engineering. Biopolymers. 2008;89(5):380-91.
110. Rajadas J, Liu CW, Novick P, Kelley NW, Inayathullah M, LeMieux MC, et al. Rationally Designed Turn Promoting Mutation in the Amyloid-beta Peptide Sequence Stabilizes Oligomers in Solution. Plos One. 2011;6(7).
111. Riek R, Hornemann S, Wider G, Billeter M, Glockshuber R, Wuthrich K. NMR structure of the mouse prion protein domain PrP(121-231). Nature. 1996;382(6587):180-2.
112. Damberger FF, Christen B, Perez DR, Hornemann S, Wuthrich K. Cellular prion protein conformation and function. Proceedings of the National Academy of Sciences of the United States of America. 2011;108(42):17308-13.
113. Kurt TD, Bett C, Fernandez-Borges N, Joshi-Barr S, Hornemann S, Rulicke T, et al. Prion transmission prevented by modifying the beta2-alpha2 loop structure of host PrPC. The Journal of neuroscience : the official journal of the Society for Neuroscience. 2014;34(3):1022-7.
114. Nelson R, Sawaya MR, Balbirnie M, Madsen AO, Riekel C, Grothe R, et al. Structure of the cross-beta spine of amyloid-like fibrils. Nature. 2005;435(7043):773-8.

Table 1. Kinetic parameters of HuPrP aggregation in presence of various BPMs. The sigmoidal fit as per given equations (see methods) was used to calculate the kinetic parameters. Since the lag phase and T_{50} in case of **B8** and **B9** samples were too long to be accurately determined, they are denoted as N.D. In all cases, average value and standard deviation of fluorescence assays (1:3 molar ratio) performed in triplicates are shown.

	Lag-time (h)	T_{50} (h)	$Intensity_{max}$
HuPrP	23.8±1.4	32.4±0.9	162.5±6.8
B1	12.4±2.5	29.4±1.6	377.5±25.8
B2	11.1±3.2	29.9±2.1	384.1±32.6
B3	24.9±1.2	35.1±0.8	127.9±7.1
B4	31.2±0.6	39.2±0.4	106.4±3.4
B5	38.7±0.4	43.1±0.2	117.6±2.6
B6	12.3±3.1	32.1±1.9	276.5±21.9
B7	11.8±2.1	26.6±1.3	248.8±14.3
B8	N.D.	N.D.	15.7±8.1
B9	N.D.	N.D.	10.24±4.6
B10	18.8±1.8	31.7±1.2	188.1±9.6
B11	22.5±1.8	33.5±1.1	190.7±12.4

Table 2. Apparent dissociation constant and binding free energies of HuPrP with different BPMs obtained from fluorescence binding experiments. In all cases, average value and standard deviation of fluorescence assays performed in triplicates are given.

Ligand	N	Apparent K_d (uM)	$\Delta G_{binding}$ (kcal/mol)
B1	0.86±0.09	0.64±0.07	-8.5±0.9
B5	0.87±0.14	1.03±0.19	-8.2±1.5
B6	0.90±0.27	1.8±0.13	-7.8±0.5
B9	0.84±0.14	0.34±0.04	-8.8±1.03

FIGURE 1

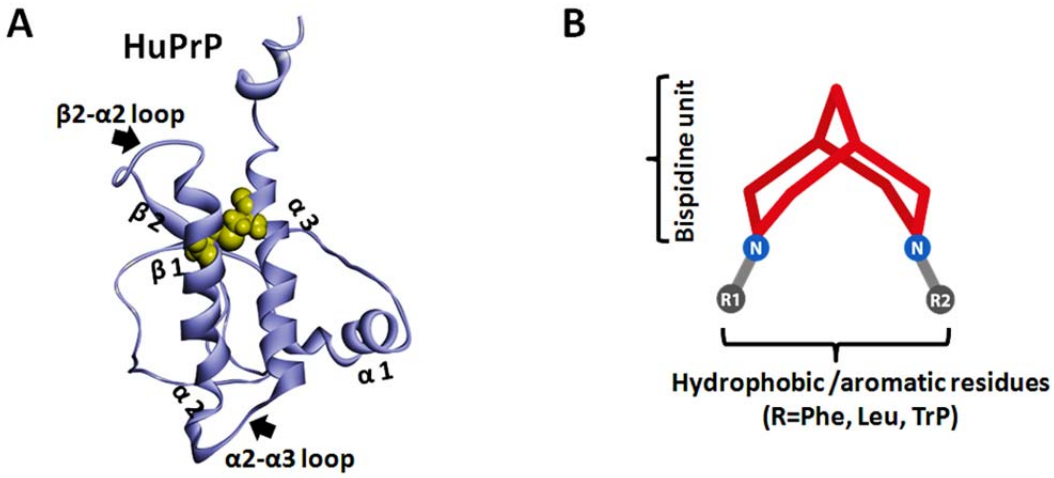

FIGURE 1. Structural representations of human prion protein and Bispidine based peptidomimetics (A) Structure of human prion protein (PDB id: 2 KUN) depicting different secondary structural components *i.e.* helix 1(α1), helix 2(α2), helix 3(α3), beta-sheet 1(β1) and beta-sheet 2(β2). The positions of β2-α2 loop (residues 166-172) and α2-α3 loop (residues 190-200) are shown by black arrows. The Cys residues 179 and 214 forming disulphide bond in the native HuPrP structure are shown in space-filling (yellow). (B) Structure of Bispidine based peptidomimetics (BPMs). Bicyclic rigid bispidine unit is shown with conjugated amino acids represented as R1 and R2. The residue side chains and protecting groups were varied to produce a series of BPMs.

FIGURE 2

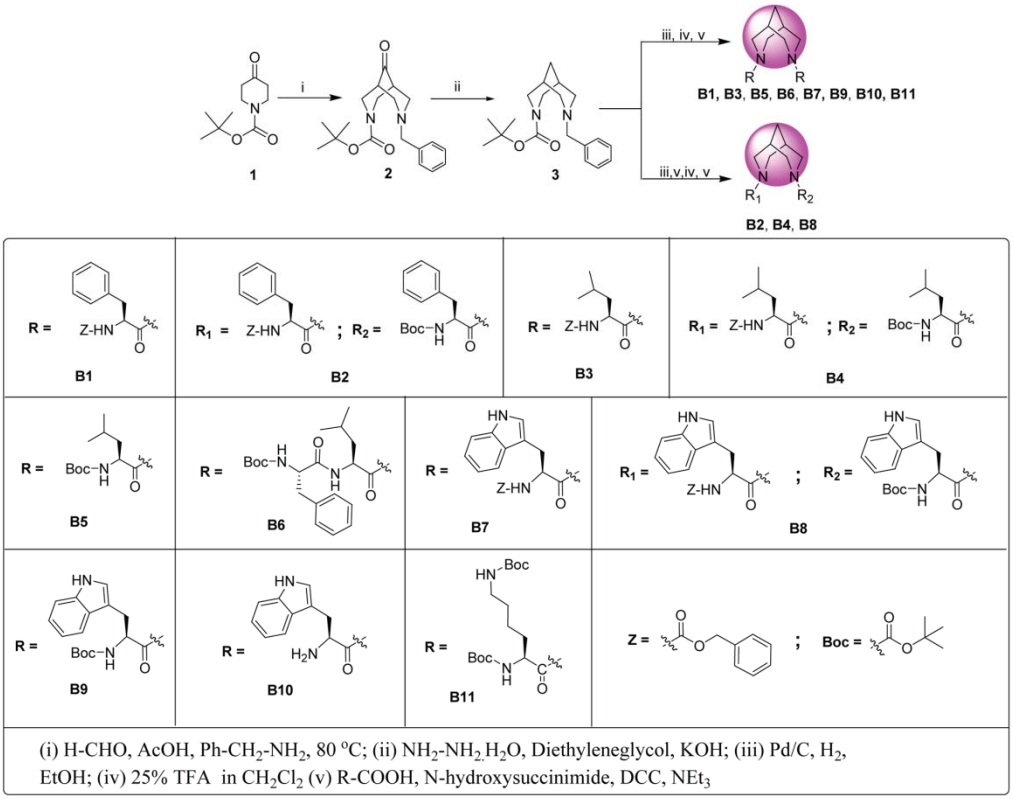

FIGURE 2. Synthesis and structure of Bispidine peptidomimetics. All the bispidine-based peptidomimetics (BPMs) were synthesized by typical peptide coupling reaction between bispidine scaffold and N-protected amino acids. The protected bispidine 3 was synthesized from Boc-protected piperidone 1. A double Mannich reaction of 1 with benzylamine and formaldehyde yielded bispidinone 2, which was reduced by Wolff-Kishner reaction yielding 3. The protected bispidine derivative was functionalized with appropriate N-protected amino acids to obtain a variety of BPMs (**B1**-**B11**).

FIGURE 3

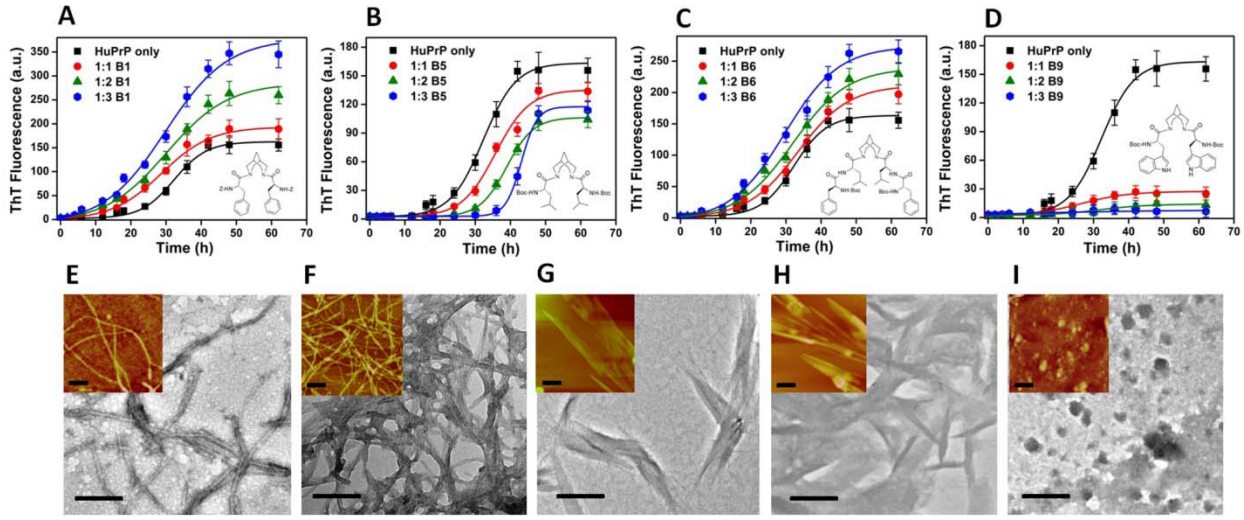

FIGURE 3. Prion amyloid kinetics and morphology in the presence of BPMs. Changes in ThT fluorescence were plotted as a function of time to represent the aggregation kinetics of HuPrP alone (black trace) and in the presence of varying concentrations of different BPMs (colored traces). The aggregation kinetics of HuPrP alone followed a sigmoidal trend. (A) A dose dependent augmentation in ThT fluorescence in the presence of Phe-BPM **B1**. (B) Subnormal ThT kinetics in the presence of increasing concentrations of Leu-BPM **B5**. (C) Accelerated ThT kinetics in the presence of increasing molar concentrations of **B6** (Phe/Leu-BPM), indicating a reversal of the delay effect observed in presence of Leu-BPMs. (D) Abrogated ThT response in the presence of different molar concentrations of **B9** (Trp-BPM). The TEM and AFM images of (E) control HuPrP fibrils, (F) dense fibrillation in the presence of **B1**, (G) thin and laterally aligned fibrils formed in the presence of **B5**, (H) densely populated thick and laterally aligned short fibers formed in the presence of **B6** and (I) unstructured and non-fibrillar aggregates formed in the presence of **B9**. The TEM and AFM images of different aggregates were recorded after incubating HuPrP (30 μM) for 60 h with 3.0 molar equivalents of respective BPMs. Scale Bars represent 500 nm and 200 nm for TEM and AFM images (inset) respectively.

FIGURE 4

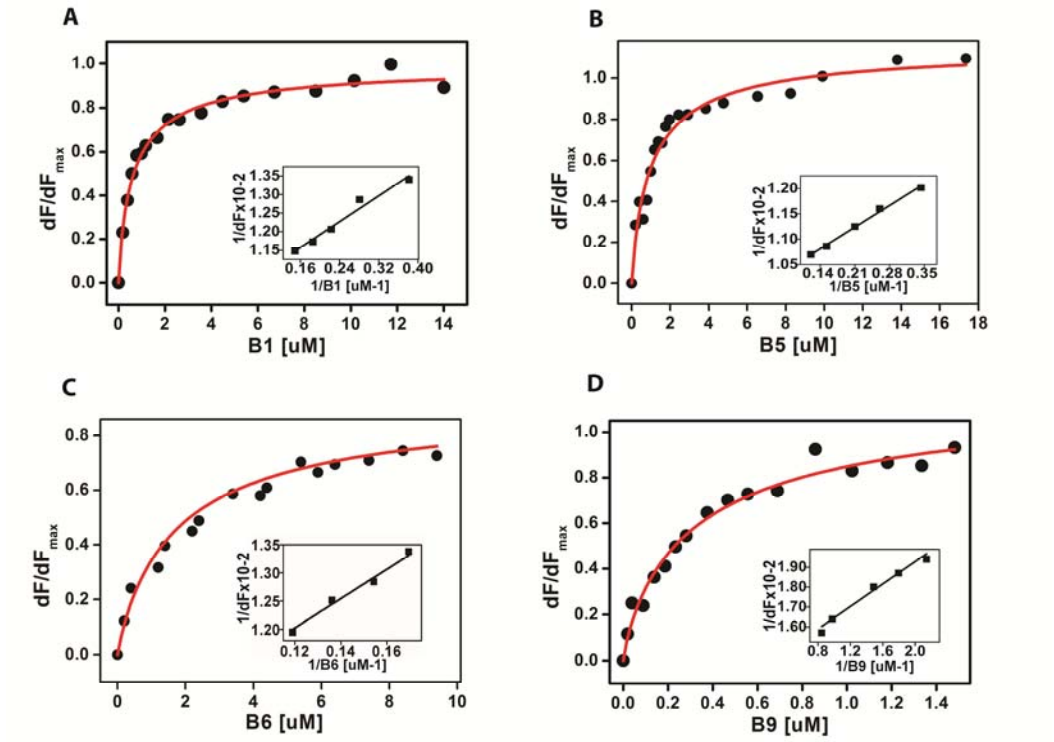

FIGURE 4. Ligand interaction estimation by fluorescence binding assay. The binding of ligands (BPMs) with HuPrP are shown in the plot of dF/dF_{max} (Fraction bound) versus the concentrations of BPMs; (A) **B1**, (B) **B5**, (C) **B6** and (D) **B9** as obtained from the fluorescence binding experiments. In each case, inset shows the linear double-reciprocal plot of 1/dF versus 1/(concentration of BPM), extrapolated to the ordinate for obtaining the dF_{max} value from the intercept. The slope/intercept in each binding curve gives the apparent dissociation constant (K_d). The concentration of HuPrP was kept at 5 μM in each case.

FIGURE 5

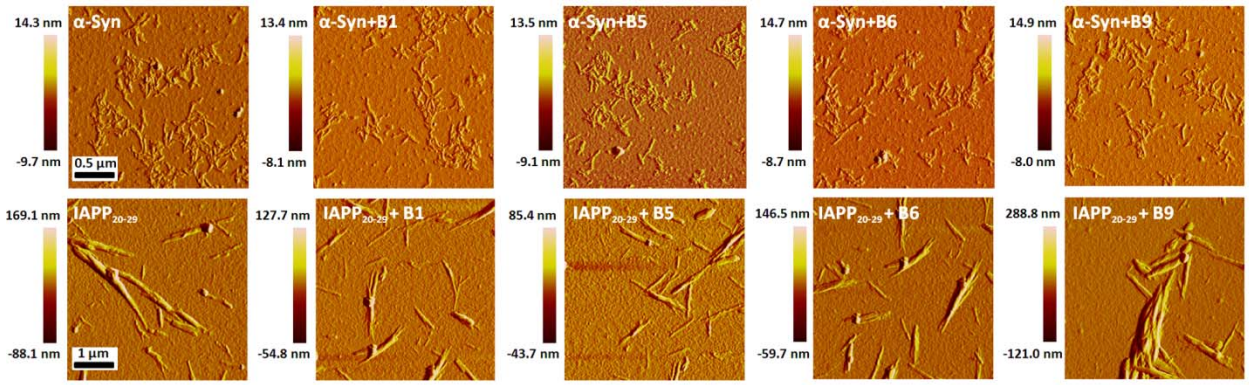

FIGURE 5. Effect of BPMs on α-Synuclein and $IAPP_{20-29}$ amyloid aggregation. The AFM images of α-Synuclein and $IAPP_{20-29}$ aggregates formed in presence of different BPMs. The gross fibrillar morphology in both cases remained unperturbed in the presence of BPMs **B1**, **B5**, **B6** and **B9** as compared to the control samples without any added BPM. While α-Synuclein fibrils were thinner and short (~12-16 nm), $IAPP_{20-29}$ formed large and bulky (~120-200 nm) fibrillar aggregates plausibly resulting from lateral alignment. The images were recorded after incubating α-Synuclein and $IAPP_{20-29}$ (both 100 µM) in aggregation conditions for 150 h and 50 h respectively with 3.0 molar equivalents of respective BPMs. Scale Bars represent 500 nm and 1 µm for α-Synuclein and $IAPP_{20-29}$ images respectively.

FIGURE 6

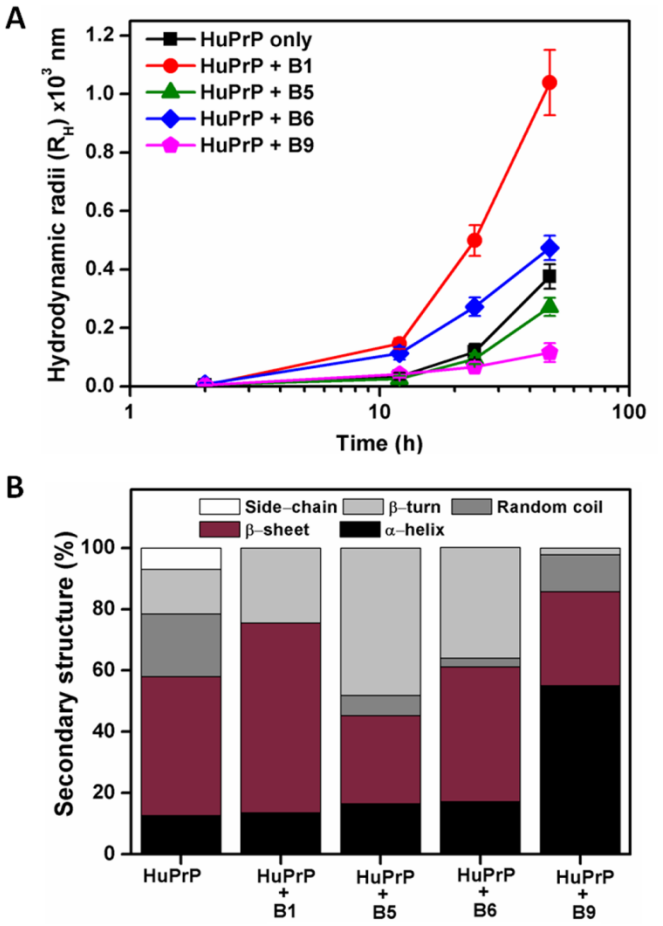

FIGURE 6. Particle size distribution and secondary structure content of aggregates. Average particle size of HuPrP aggregates plotted as variations of hydrodynamic radii versus time. (A) The size of oligomers increased substantially in the presence of **B1** and **B6** (red and blue traces, respectively) as compared to HuPrP control (black) indicating acceleration effect of these BPMs. Presence of **B5** (green) showed slow increase in aggregate size whereas in the presence of **B9** (magenta), consistently low particle sizes were observed. (B) The variations in secondary structural elements in each aggregate type were monitored by ATR-FTIR and presented as percentage of total secondary structural content of HuPrP. A substantial increase in β-sheet content in the presence of **B1** as compared to HuPrP alone is evident, affirming higher fibrillar content. **B5** containing samples displayed low β sheet and high β turn content. High α-helical content was detected in presence of **B9**, suggesting very low or no amyloid content.

FIGURE 7

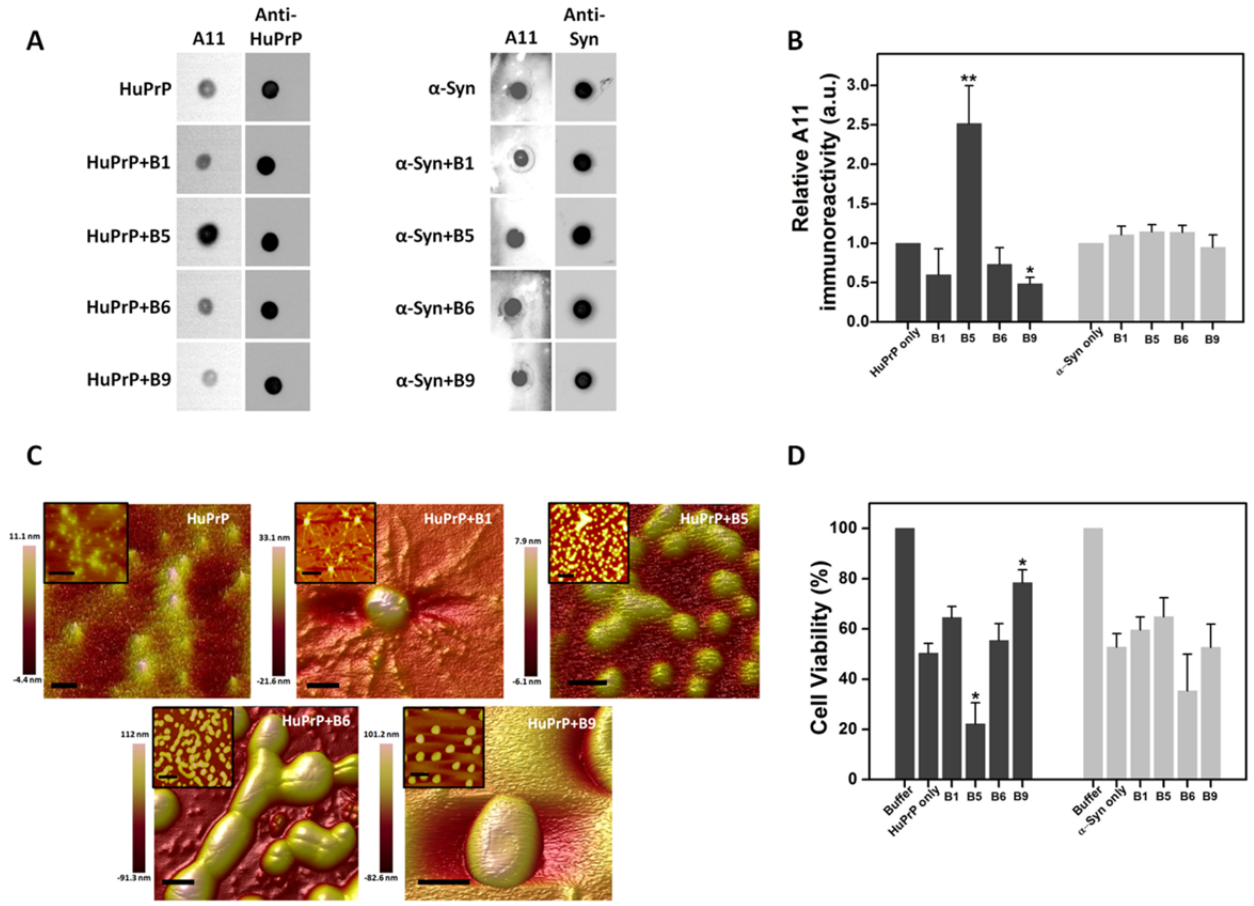

FIGURE 7. Toxic oligomer detection and morphology assessment. (A) A11 antibody dot blot analysis of HuPrP and α-Synuclein (α-Syn) oligomers formed in presence and absence of BPMs. Loading controls are also shown using HuPrP specific and α-Synuclein specific antibodies. (B) Analysis of the variation in the intensities of dot blots. The data indicates differences in immunoreactivity of the oligomer-specific A11 antibody to different aggregates. The **B5** induced aggregates showed the presence of significantly higher proportions of toxic oligomers as compared to others ($p<0.01$). HuPrP alone, **B1** and **B6** samples showed similar immunoreactivities whereas, **B9** samples showed least A11 immunoreactivity ($p<0.05$). (C) The corresponding AFM images showing distinct morphological features of HuPrP oligomers induced by the presence of different BPMs. Presence of **B1** resulted in oligomers with radiating fibrillar extremities, **B5** produced oligomers of smaller dimension (~5-6 nm) as compared to control HuPrP (~10-11nm), **B6** induced the coalescence of oligomers, forming large pre-fibrillar aggregates and B9 induced the formation of large, distended oligomers. Scale Bars represent 200 nm (1 µm for inset). (D) Cytotoxicity assessment of oligomers. SH-SY5Y cells were incubated for 24 hours with HuPrP oligomers, α-Synuclein oligomers alongside different BPM-induced oligomers and cell viabilities were measured using MTT assay. In each case a 1:3 molar ratio of HuPrP/ α-Synuclein to BPM was maintained with final HuPrP and α-Synuclein concentration in each case kept at 0.5 µM and 1.5 µM respectively (~50% cell viability). Oligomers formed in presence of B1 and **B6** resulted in marginally reduced cellular toxicity; **B9**-mediated oligomers exhibited significantly lowered cell toxicity whereas **B5**-induced oligomers were the most toxic ($p<0.05$). In case of α-Synuclein, the oligomers formed in presence of different BPMs showed no significant change in cellular toxicities as compared to control

synuclein oligomers (~50% cell death). The reduction in MTT is plotted as percentage cell viability of SH-SY5Y cells. The viability of cells incubated with phosphate buffer, pH 7.0 only is taken as 100%. The error bars correspond to standard deviations of six data sets. Statistical significance was evaluated using two-tailed t-test ((*p < 0.05, **p < 0.01, ***p< 0.001).

FIGURE 8

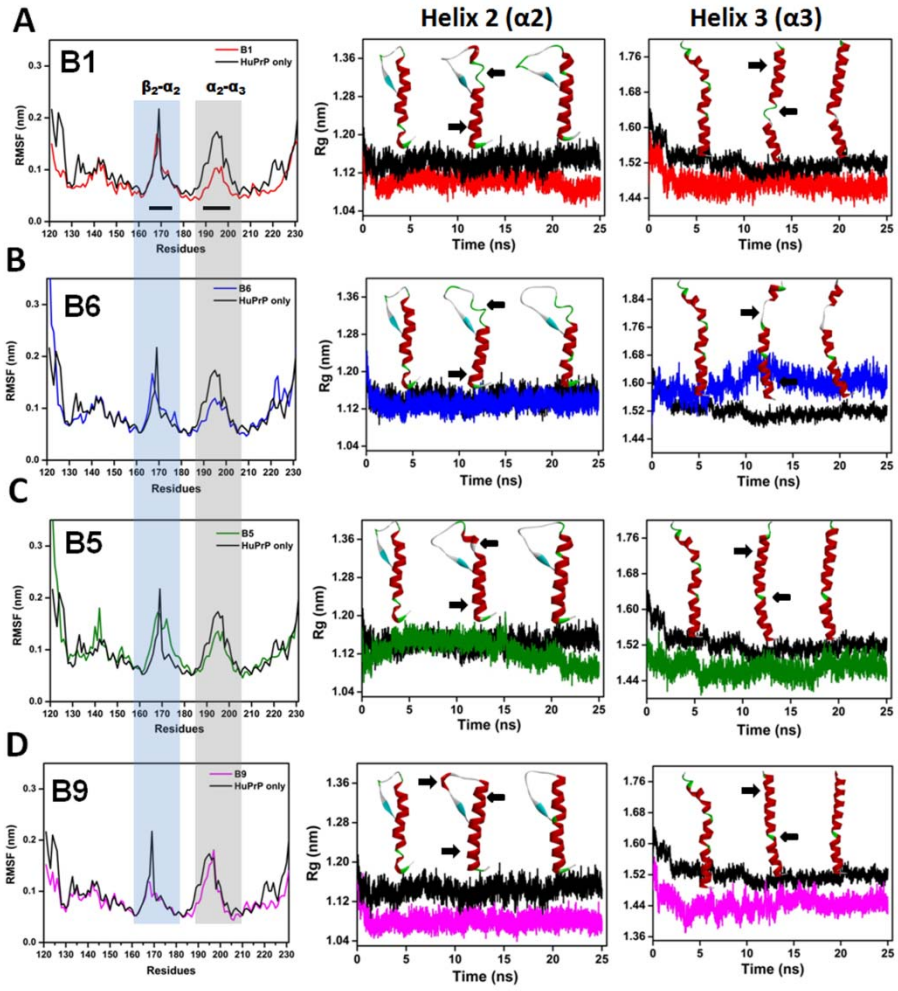

FIGURE 8. Molecular interactions of BPMs with the HuPrP structure. In each case, variations in HuPrP alone (black), **B1** (red), **B6** (blue), **B5** (green) and **B9** (magenta) complexes are represented in color traces. Left panels showing residue wise RMSF plots; A) **B1** and B) **B6** complexes exhibiting β2-α2 loop mobilities centered at Tyr 169 and lowered α2-α3 loop mobility, C) **B5** complex showing distributed β2-α2 loop mobility and lowered α2-α3 loop mobility, D) **B9** complex depicting significantly reduced β2-α2 loop mobility and α2-α3 loop mobility matching HuPrP alone. Middle panels showing plots of radius of gyration (R_g) corresponding to α2 helix in all complexes. Corresponding MD snapshots of α2 helix taken at 5, 10 and 20 ns are also shown. A) **B1** and B) **B6** complexes showing R_g variations marginally lowered and similar to HuPrP (α 2 loop) alone respectively. In both cases, helix-coil-helix transitions near the disulphide linkage and helix reorganization near the N-terminal end are seen (black arrows). C) **B5** and D) **B9** complexes showing marginally and significantly lowered R_g variations respectively. In both

cases, helix reorganization near the N and C-terminal is seen and helix-coil-helix transitions were absent (black arrows). An extra helical component stabilizing β2-α2 loop is also seen in **B9** complex (black arrow). Right panels showing R_g plots of α3 helix in all complexes. Corresponding MD snapshots of α3 helix taken at 5, 10 and 20 ns are also shown. A) **B1** ,C) **B5** and D) **B9** complexes showing R_g variations lowered compared to HuPrP (α3 loop) alone. A helix-coil-helix transition near the disulphide linkage is prominently observed only in **B1** complex and is absent other complexes. All complexes showed helix reorganization near the C-terminal end. B) **B6** complex showing remarkable increase in R_g after 5 ns validating the observed helix unfolding at the C-terminal end (black arrow).

FIGURE 9

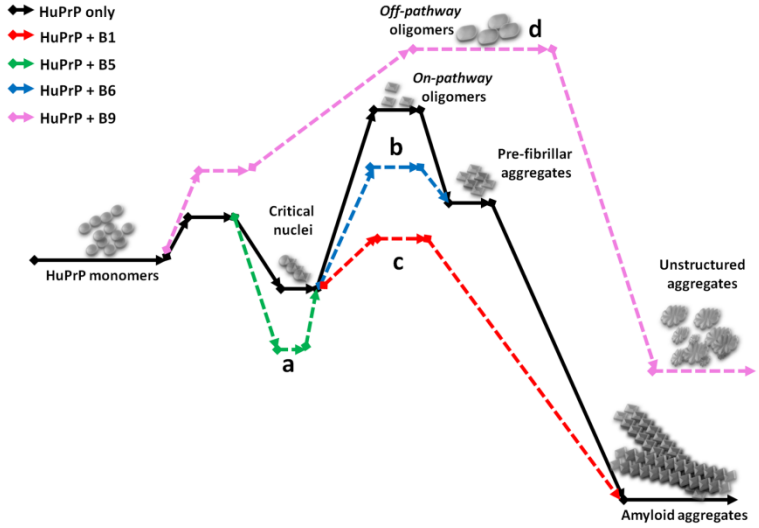

FIGURE 9. Prion assembly and BPM remodeling pathways. The black arrows represent major steps in the *on-pathway* amyloid conversion of HuPrP. Subsequent modifications in presence of different BPMs are shown as colored arrows. a) Delay in critical nucleation in case of **B5** (green arrows); b) Reduction of energy barrier for the formation of pre-fibrillar aggregates in presence of **B6** (blue arrows); c) Lowering of energy barrier of on-pathway oligomerization and pre-fibrillar aggregates in presence of **B1** (red arrows) and d) *Off-pathway* oligomerization ending into unstructured aggregates in presence of **B9** (magenta arrows).